International Journal of Fatigue 66 (2014) 138–154

Contents lists available at ScienceDirect

International Journal of Fatigue

journal homepage: www.elsevier.com/locate/ijfatigue

Ratcheting behaviour of high strength rail steels under bi-axial compression–torsion loadings: Experiment and simulation

Chung Lun Pun [a], Qianhua Kan [b], Peter J. Mutton [c], Guozheng Kang [b], Wenyi Yan [a,*]

[a] Department of Mechanical and Aerospace Engineering, Monash University, Clayton, VIC 3800, Australia
[b] Department of Applied Mechanics and Engineering, Southwest Jiaotong University, Chengdu 610031, People's Republic of China
[c] Institute of Railway Technology, Monash University, Clayton, VIC 3800, Australia

ARTICLE INFO

Article history:
Received 9 September 2013
Received in revised form 19 March 2014
Accepted 21 March 2014
Available online 3 April 2014

Keywords:
High strength rail steel
Ratcheting
Non-proportional loading path
Cyclic loading

ABSTRACT

Experimental studies were carried out to investigate the ratcheting behaviour of three high strength rail steels of similar nominal hardness but with different chemical compositions subjected to uniaxial and non-proportionally bi-axial compression–torsion cyclic loading conditions. Different axial stress and equivalent shear stress amplitudes and different non-proportional loading paths were considered. Experimental results show that an obvious cyclic softening (i.e., the stress amplitude decreases with the increase of cyclic number) occurs in all three steels under uniaxial strain cycling. The ratcheting strain and ratcheting strain rate increase with the axial stress and the equivalent shear stress amplitudes under bi-axial compression–torsion stress cycling. Moreover, both ratcheting strain and ratcheting strain rate are strongly influenced by the non-proportional loading path. Among the three rail steels, it is found that the low alloy heat-treated rail steel grade has a better resistance to ratcheting than the two hypereutectoid rail steel grades. The hypereutectoid rail steel grade with a higher carbon content gives a lower ratcheting strain and a lower ratcheting strain rate than the hypereutectoid rail steel grade with a lower carbon content under higher loading amplitude. To simulate the ratcheting behaviour of the high strength rail steels, an existing cyclic plasticity model was modified by coupling a non-proportionally multi-axial parameter into isotropic softening and kinematic hardening rules. The method to calibrate the material parameters for the plasticity model and the simulated results validated with experimental data for the three studied rail steels are presented in the paper. This modified plasticity model with the calibrated material data from the experimental study can be applied to investigate the ratcheting behaviour of the three rail steels under wheel–rail cyclic rolling contact in practice.

1. Introduction

In an actual wheel–rail rolling contact process, the rail is subjected to cyclic loading and the rail surface is subjected to rolling and sliding and relatively high contact stresses. It has been found that the cyclic stresses and the plastic deformation are the major factors influencing the rail degradation processes [1,2]. The stresses endured by the rail are always multiaxial, non-proportional and randomly fluctuating in magnitude and direction [3]. If the wheel–rail contact conditions result in a stress level above the plastic shakedown limit or ratcheting threshold, new plastic deformation will occur and accumulate, i.e., ratcheting occurs, under each cycle of loading. Although the plastic deformation in the rail in each cycle may be very small, the plastic deformation accumulates to large values over many cycles of loading [4]. When the ratcheting strain reaches the limiting ductility of the rail, the rail will fail at the local material point, which corresponds to the initiation of wear or rolling contact fatigue [5–7], e.g., in the form of head checks in the rail head. This states that plastic ratcheting plays a key role in causing the rolling contact failure of the rail, i.e. wear and rolling contact fatigue damage. Additionally, the demanding conditions imposed by rail transport of higher axle loads, higher train speeds and increasing annual haulage rates lead to increasing the rate of rail degradations and the risk in maintainability and the operational safety of the rail. To prevent any catastrophic failure of rail from the demanding conditions, it is essential to investigate the ratcheting behaviour and to quantify the cyclic plasticity in the rail head of the rails available today. Consequently, the investigation should provide useful information to the development and application of rail steels and the development of effective rail maintenance strategies in order to mitigate rail degradation.

* Corresponding author. Tel.: +61 3 990 20113; fax: +61 3 9905 1825.
E-mail address: wenyi.yan@monash.edu (W. Yan).

http://dx.doi.org/10.1016/j.ijfatigue.2014.03.021
0142-1123/

Study of ratcheting has been one of the attractive research fields in the last three decades. Extensive studies have revealed that the cyclic deformation characteristic of materials subjected to uniaxial and multiaxial cyclic loadings can be demonstrated in strain-controlled loading histories. Under such loading conditions, materials can feature cyclic hardening, cyclic stable or cyclic softening. Stephens et al. [8] stated that the tendency for cyclic softening/hardening of a material is influenced by its microstructure, i.e. the density and arrangement of the dislocation structure and substructure of the material. This relationship was also demonstrated in the studies by Sunwoo et al. [9] and Krishna et al. [10]. Furthermore, it has been found that the ratcheting behaviour of a material is strongly dependent on its cyclic deformation characteristics [11,12].

Under unsymmetrical stress-controlled cyclic loading tests, the induced hysteresis loops never close and the strain gradually accumulates, i.e. strain ratcheting occurs. This is one of the important plastic deformation phenomena of materials subjected to cyclic loading [13,14] and so the uniaxial and multi-axial stress-controlled cyclic loading tests have been widely applied to investigate the uniaxial and multiaxial ratcheting behaviours of various materials, which include ZK60 Mg alloy [15], 42CrMo steel [16,17], SS304 stainless steel [11,12,18–21], 1020 and 1026 carbon steels [22,23], 1045 steel [24,25], 1070 steel [26,27], 316 stainless steel [28–30] copper and copper alloy [31–33], ordinary and heat-treated rail steels [31,34] and U71Mn rail steel [35,36]. These experimental studies revealed that the uniaxial and multiaxial ratcheting behaviour of the materials are strongly influenced by the mean stress, stress amplitude, loading path and loading history.

Although extensive studies have been carried out to investigate the ratcheting behaviour of different materials, limited ratcheting studies were conducted on the in-service high strength rail steels [31,34–36]. Bower [31] conducted tension–torsion stress cycling tests to study the ratcheting behaviour of an ordinary carbon rail steel. McDowell [34] carried out both uniaxial and bi-axial tension–torsion stress cycling tests to investigate the ratcheting behaviour of an ordinary carbon rail and a heat treated high strength rail steel. Kang et al. [35,36] conducted a systematic experimental program to investigate the uniaxial and multi-axial ratcheting behaviour of the U71Mn rail steel. In these reported experiments for rail steels and also other materials, it was found that different materials exhibit different ratcheting behaviours and varying material characteristics. Furthermore, the ratcheting behaviour of the materials in the reported experimental studies was mostly investigated under uniaxial or tension–torsion multi-axial loadings. In the case of rail steel, the bi-axial cyclic compression–torsion test is one of the most appropriate methods to simulate the loading experienced by rail steel in the rail head due to rolling contact between the wheel and the rail. A thorough literature search indicates that the ratcheting behaviour of the currently-available high strength rail steel grades has not been experimentally investigated. The current effort is therefore the first to investigate the ratcheting behaviour of three new high strength rail steels which are currently used in heavy haul railways in Australia. The three rail grades selected are of similar nominal hardness, but differ in chemical composition, which enables to examine the influence of alloy design on the resistance to ratcheting of the rail.

To quantify the ratcheting behaviour in the rail head accurately, a cyclic plasticity constitutive model, which reasonably describes the ratcheting behaviour, should be applied to simulate the rolling contact between the wheel and the rail. Extensive studies on cyclic plasticity constitutive models have been conducted for more than 30 years. The well-known models, which couple the isotropic and kinematic hardening rules to simulate the ratcheting behaviour, include the Chaboche model [37–39] and the Ohno–Wang model [40]. The capability of these models for predicting ratcheting was reviewed by Ohno [41] and Bari and Hassan [42]. One of the major problems of these models is the inappropriate prediction of ratcheting in multiaxial loading cases due to the coupled calculation of plastic modulus with the kinematic hardening rule through the consistency condition [42,43]. Bari and Hassan [43] identified that the direction and the magnitude of the normal direction of the yield surface translation continuously changes under multiaxial loading, which is dictated by the kinematic hardening rule, while these remain unchanged throughout the uniaxial loading history. This indicates that an appropriate evolution rule of kinematic hardening is of paramount importance for accurate multiaxial ratcheting prediction.

To improve the capability of the model for multiaxial ratcheting prediction, many studies were carried out to modify existing coupled models or the kinematic hardening rules. McDowell [34] and Jiang and Sehitoglu [44] modified the Ohno–Wang model [40]. Voyiadjis and Basuroychowdhury [45] incorporated the stress-rate direction in the kinematic hardening rule proposed by Chaboche [38]. However, it was found that these modifications cannot improve the accuracy of the multiaxial ratcheting prediction [43]. AbdelKarim and Ohno [46] combined the nonlinear Armstrong and Frederick kinematic hardening rule [47] and the Ohno and Wang rule [40] through a bi-axial parameter with small value. Bari and Hassan [43] superposed the Chaboche model [38] upon the Burlet–Cailletaud model [48] by introducing a new ratcheting parameter. It was demonstrated that the introduction of the bi-axial parameter in the kinematic hardening rule can significantly improve the accuracy of multiaxial ratcheting prediction. Döring et al. [49] developed a new kinematic hardening rule which considers the influence of non-proportional factor on multiaxial ratcheting. Chen et al. [50] also developed a new kinematic hardening model to describe the non-proportionally multiaxial ratcheting based on the Ohno–Wang model [40]. Both of these models can reasonably simulate non-proportionally multiaxial ratcheting. Despite this, all these models have not considered the effects of cyclic hardening/softening feature, temperature factors, and time-dependent factors. Kang et al. [51] extended the Ohno–Wang model to consider the influence of strain-amplitude-dependent and non-saturated cyclic hardening on uniaxial ratcheting. The AbdelKarim and Ohno model [46] was modified by Kang et al. [52], who introduced the temperature-dependent parameters in the kinematic hardening rule to consider the effect of dynamic strain aging on uniaxial and multiaxial ratchetting at high temperature. Taguchi and Takahashi [53] developed a constitutive model based on Ohno–Wang model [40] to describe the cyclic softening feature of the material and Kan et al. [54] proposed a model to describe the cyclic hardening feature of the material.

Although many cyclic plasticity constitutive models for ratcheting simulation have been developed, it is still challenging to find a generic and precise constitutive model due to the complexity of ratcheting behaviour. Additionally, extensive studies of ratcheting have demonstrated that different materials exhibit different ratcheting behaviour and varying material characteristics. This indicates that the existing models may not be reasonably and simultaneously describe the deformation characteristics of the high strength rail steels studied herein. Therefore, based on the experimental results, which will be demonstrated in Section 2 of this paper, and in the framework of unified plasticity, a cyclic plasticity constitutive model for non-proportionally multiaxial ratcheting is developed by modifying the AbdelKarim and Ohno model in current study. The cyclic deformation characteristics of the materials are taken into account and the influence of non-proportionality of loading path on multiaxial ratcheting is reflected by introducing a non-proportional factor. Additionally, it has been found that an appropriate method to calibrate the material parameters required

Table 1
Chemical composition of the three high strength rail steels.

Rail type	C	Si	Mn	P	S	Cr
HE1	1.0	0.5	0.7			0.2
HE2	0.85	0.55	0.55	0.014	0.005	
LAHT	0.8	0.7	0.95			0.4

for the cyclic plasticity constitutive model is important for accurate multiaxial ratcheting simulation. A detailed methodology of how to calibrate the material parameters of those three studied rail steels required for the developed model are presented. The developed model with the calibrated material parameters is applied to simulate the uniaxial and multiaxial ratcheting of the studied rail steels and compared to the corresponding experimental results.

The structure of this paper is as follows: the details of the materials, specimens and experimental procedures as well as the experimental results of monotonic tensile tests, uniaxial strain cycling and bi-axial compression–torsion stress cycling are presented and discussed in Section 2. The numerical simulation of the ratcheting behaviour is presented in Section 3, which includes the modification of an existing cyclic plasticity model, the method to calibrate the material parameters required by the modified constitutive model and the results of the numerical simulation. Conclusions are given in Section 4.

2. Experimental study

2.1. Materials and specimens

The materials studied herein are three new high strength pearlitic rail steels which are currently used in heavy haul railways in Australia. They are a low alloy heat-treated (LAHT) grade with carbon content of 0.8% and two hypereutectoid grades with carbon content respectively of 1% (HE1) and 0.85% (HE2). The chemical composition of these three rail steels is given in Table 1. All the three rail steels were of similar nominal hardness of 400–420 HV measured at the top of the rail head as shown in Fig. 1(a). All these three rail steels were also included in a larger range of rail steels subjected to a detailed program of laboratory and in-service testing by Szablewski et al. [55,56].

Two sets of specimens, round solid specimens and thin-walled tubular standard specimens, were prepared for each material. Monotonic tensile tests and uniaxial strain cycling tests were performed on the round solid specimens which have a test section diameter of 5 mm and length of 30 mm while bi-axial compression–torsion tests were performed on the thin-walled tubular specimen with an outer diameter of 16 mm, an inner diameter of 13 mm, and a length of 30 mm in the test section. The machining process started with extraction of solid bars from the head of new 68 kg/m rail samples. The position of the specimen blanks within the head of the rail took into consideration the gradient in mechanical properties typically present in heat treated grades, as illustrated in Fig. 1(a) and (b), by the hardness distribution measured in the current grades. The location of the round solid specimens and the thin-walled tubular specimens in the cross-section of the rail head, which are illustrated in Fig. 2(a) and (b), respectively, therefore corresponded to a region of relatively uniform hardness in each of the steels, see Fig. 1(a). In addition, the mean hardness in the region was similar for all three steels, as illustrated in Fig. 1(b) by the hardness distribution measured in an annulus corresponding to the gauge length of the tubular specimen. It is worth noting that the definition of angular displacement θ from the gauge corner of the rail head as shown in

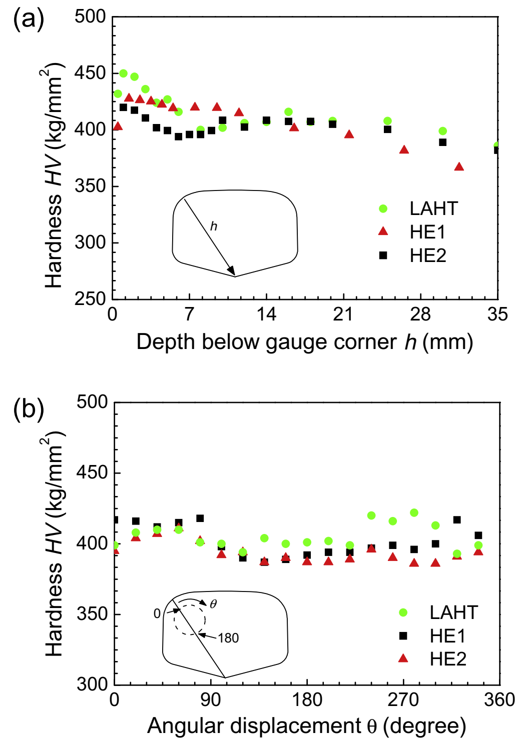

Fig. 1. Hardness distribution measured in the three rail steels at (a) the depth below gauge corner and (b) clockwise angular displacement θ from gauge corner position of the rail head.

Fig. 1(b) is illustrated by the red[1] solid line in Fig. 2(b). The bars were then turned to finalize the specimen's geometry while the hole in thin-walled tubular specimens was made by the deep hole drilling operation at Metal Drilling Pty Ltd. in Australia before the geometry was finalized. Specimens were finally polished with a fine emery paper. No thermal treatment was performed in the specimen preparation.

2.2. Experimental program

All tests were conducted at room temperature by employing a servo-valve controlled electro-hydraulic testing machine MTS809-250 kN, which has the capacity to control axial force and torque independently. An extensometer with an axial strain limit of ±10% was employed in the monotonic tensile tests and the uniaxial strain cycling tests while a tension–torsion extensometer with 25 mm gauge length and axial strain limit of ±10% and shear angle limit of ±5° was employed in the bi-axial compression–torsion tests to measure the axial elongation and torsional angle. Loading rates of strain cycling and stress cycling were 0.2% s^{-1} and 200 MPa s^{-1}, respectively. The loading stopped at 100 cycles in all cases because a quasi-steady ratcheting rate was obtained and the coupling between ratcheting and damage could be avoided. (Note that the current study focuses on the ratcheting behaviour only.) In this paper, the axial stress was determined as axial force per unit cross-section area while the axial force and axial strain were directly obtained from the Teststar II control system and the extensometer, respectively. The shear stress and the shear strain were determined respectively from the torque and the torsional angle which were measured by the control system.

[1] For interpretation of colour in Figs. 2 and 4, the reader is referred to the web version of this article.

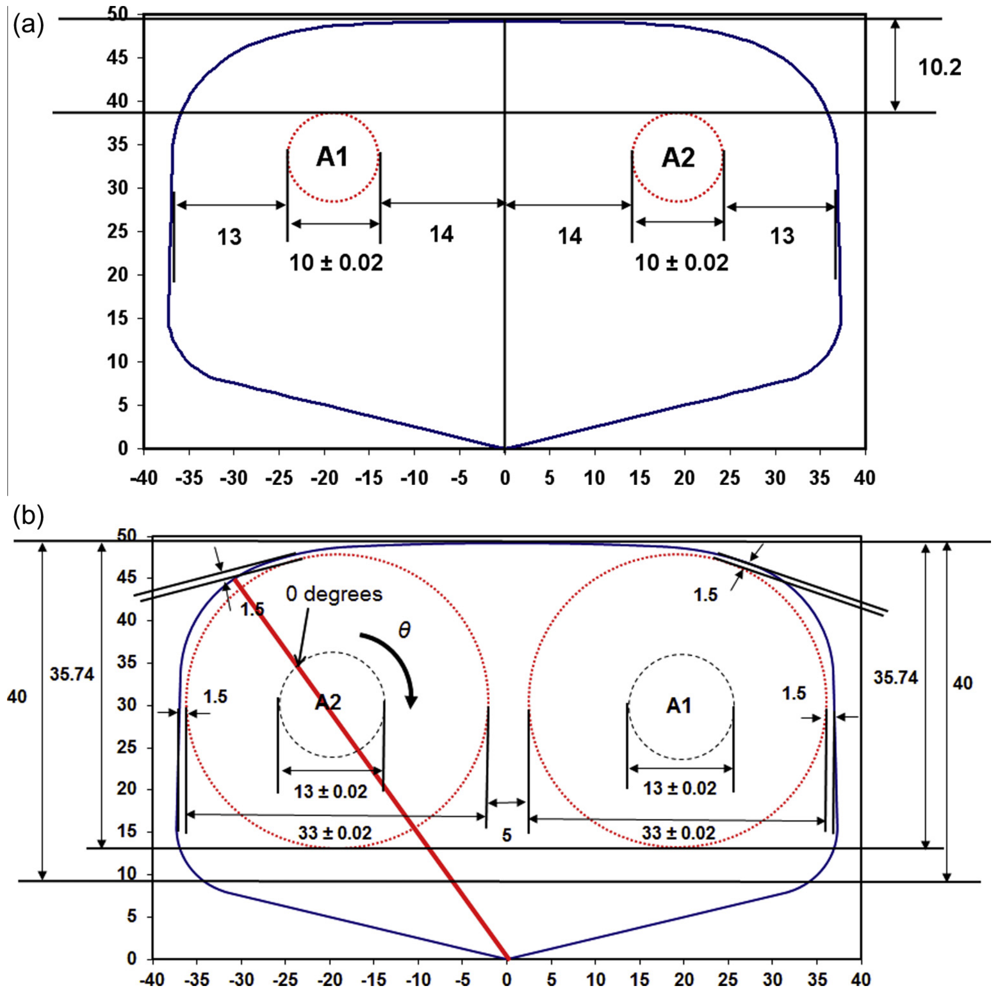

Fig. 2. Location of (a) round solid specimen and (b) thin-walled tubular specimen in the rail head.

The initial tests involved monotonic tensile loading condition in order to obtain some basic mechanical parameters, such as yield strength and ultimate tensile strength. Following the monotonic tensile test, the basic cyclic deformation characteristics of all the three materials under symmetrical uniaxial strain cycling was observed from the relationship between the stress amplitude σ_a and the number of loading cycles *N*. The stress amplitude was determined as a function of the maximum and minimum of axial stress σ_{max} and σ_{min} in each cycle obtained from the collected experimental data. After the symmetrical strain cycling, the ratcheting behaviour of the materials was studied under bi-axial compression–torsion stress cycling with different axial stress and equivalent shear stress amplitudes, see Table 2. Under asymmetrical stress cycling, the maximum and minimum of axial strain ε_{max} and ε_{min} and the maximum and minimum of shear strain γ_{max} and γ_{min} in each cycle were obtained from the collected experimental data. Due to the unclosed hysteresis loop produced under asymmetric stress cycling, the axial ratcheting strain ε_r and the torsional ratcheting strain γ_r, can then be determined. Ratcheting strain rates are then defined as $d\varepsilon_r/dN$ and $d\gamma_r/dN$, i.e., the increment of ratcheting strains ε_r and γ_r per cycle. The ratcheting behaviour of the materials under different loading conditions can be illustrated by the curve of ratcheting strain versus number of loading cycles *N*. To investigate the influence of multi-axial loading path on the ratcheting behaviour of the material, five loading paths as shown in Fig. 3 were adopted, where σ and $\sqrt{3}\tau$ represent the axial stress and the equivalent shear stress, respectively.

2.3. Results and discussion

2.3.1. Monotonic tensile tests

The tensile stress–strain curves for round solid specimen of all the three rail steels are shown in Fig. 4. It is worth noting that engineering stress and engineering strain are used in current study as the magnitude of the axial strain is always less than 4% in the current study. The experimental results of elastic modulus *E*, nominal yield strength $\sigma_{0.2}$, ultimate tensile strength σ_b and elongation at failure δ of all the three rail steels are summarized in Table 3. The results clearly show that the HE2 and the LAHT steels have the same measured elastic modulus of 212 GPa while the HE1 steel has a slightly lower elastic modulus of 203 GPa. Fig. 4 demonstrates that the LAHT steel gives the highest ultimate tensile strength of 1446 MPa while it is 1429 MPa for the HE1 steel and 1384 MPa for the HE2 steel. The results also show that the LAHT steel has a nominal yield strength of 1000 MPa which is 17.5% higher than the HE1 steel and 10.5% higher than the HE2 steel. Under the same loading conditions, the HE2 steel has the largest elongation of 12%, while it is 11.3% and 8.5% for the LAHT and the HE1 steels, respectively. Additionally, the reduction of area, which is the proportional reduction of the cross-sectional area of the specimen measured after fracture under the monotonic tensile test, of the three rail steels is listed in Table 3. The HE2 steel has the largest reduction of area of 39.5% while the reduction of area of the LAHT and the HE1 steels was measured as 35.87% and 14.71%, respectively. This indicates that the HE2 steel has the highest ductility

Table 2
Loading conditions of biaxial compression–torsion stress cycling tests.

Test	Axial stress, σ (MPa)	Equivalent shear stress $\sqrt{3}\tau$ (MPa)	Loading path
1	−400	0 ± 1000	Linear
2	−200	0 ± 800	Linear
3	−200	0 ± 1000	Linear
4	−316.25 ± 316.25	0 ± 800	Oblique
5	−200	0 ± 900	Linear
6	−100	0 ± 1000	Linear
7	0	0 ± 1000	Linear
8	−632.5	0 ± 800	Rectangular
9	−632.5	0 ± 800	Linear
10	−316.25 ± 316.25	0 ± 800	Butterfly
11	0	−100 ± 1000	Linear
12	−316.25 ± 316.25	0 ± 800	Elliptical

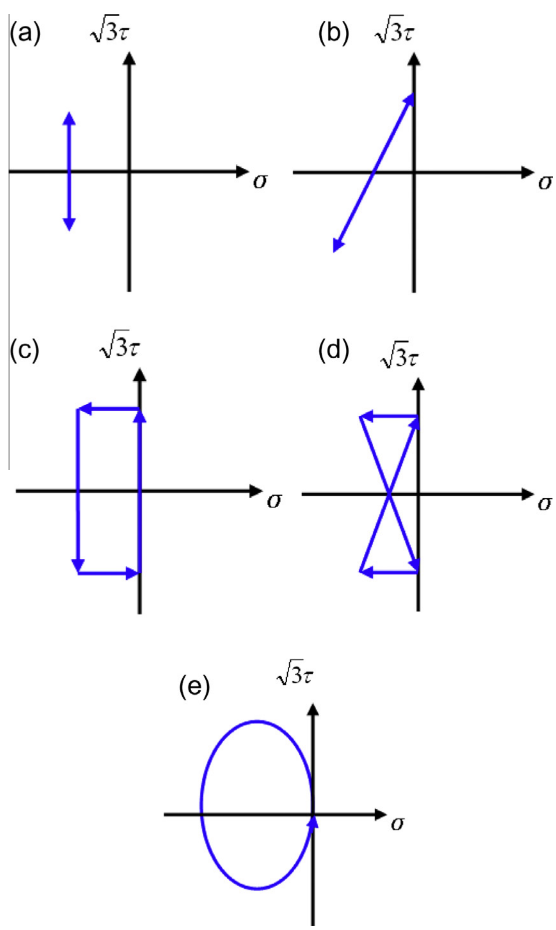

Fig. 3. Loading paths for compression–torsion stress cycling: (a) linear path, (b) oblique path, (c) rectangular path, (d) butterfly path, and (e) elliptical path.

while the HE1 steel is the least ductile one among all the three rail steels.

According to the study by Szablewski et al. [55], the nominal yield strengths of LAHT and HE2 were 930 MPa and 890 MPa, respectively, which are lower than those found in current study. However, the nominal yield strength of HE1 is 7.1% higher than in current study. Both of the ultimate tensile strengths of HE1 and HE2 were similar in these studies while the ultimate tensile strength of LAHT in current study is 3% higher than that of Szablewski et al. [55]. The elongations at failure of all the three rail steels were found to be similar. The differences in the results

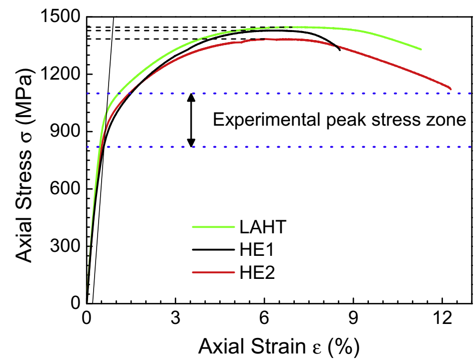

Fig. 4. Monotonic tensile stress–strain curves of the three rail steels from the round solid specimen tests.

may be due to the differences in specimen position in the rail head. The round solid specimens used in the current study were extracted from the gauge corner of the rail head, centred 18 mm from the gage side and 15 mm from the running surface, see Fig. 2(a), while the specimens used by Szablewski et al. [55] were taken from a location closer to the surfaces of the rail head, centred 12.7 mm from the gage side and 12.7 mm from the running surface, in line with the requirements for rail steels suggested by the American Railway Engineering and Maintenance-of Way Association (AREMA) [57].

Carrying out monotonic tensile tests can not only provide some basic parameters for the materials but also help the design of the bi-axial compression–torsion tests for studying the ratcheting behaviour. One of the criteria for designing the ratcheting tests is to ensure that the peak stress applied is large enough to cause plastic ratcheting. To meet this criterion, the peak stress must be higher than the yield strength of the material. However, the applied peak stress should not be too close to the ultimate tensile strength in order to avoid unexpected failure of the material in the early stage of the test. Based on these two criteria and the experimental results of all the three materials under monotonic tensile tests, the peak stress applied in the bi-axial compression–torsion stress cycling was selected in the range of 850–1100 MPa as illustrated by the blue dotted horizontal lines in Fig. 4.

2.3.2. Uniaxial strain cycling

The round solid specimens of all the three rail steels were tested under uniaxial symmetrical strain cycling at room temperature with a strain amplitude of 0.8%. The cyclic hysteresis stress–strain loops of the three rail steels under uniaxial symmetrical strain cycling are shown in Fig. 5. The results clearly show that the size of the hysteresis stress–strain loop decreases with the increase in the number of the loading cycles. Figs. 5(a) and (c) show that the tensile peak stress increases with the number of loading cycles while the compressive peak stress decreases. This issue can also be clearly identified in Fig. 6 which demonstrates the variation of the mean stress σ_m of all the three materials under uniaxial symmetrical strain cycling at different number of loading cycles.

The results clearly show that the mean stress values of both the LAHT and the HE2 steels increase with the number of loading cycles while the mean stress of the HE1 steel remains almost constant. This phenomenon may result from the difference in yield strength between these three materials, see Table 3. The HE1 steel has the lowest yield strength while the LAHT steel has the highest one among all the three rail steels. This indicates that the HE1 steel endures the lowest stress level than the LAHT and the HE2 steels under the same strain range. Furthermore, our experimental results from uniaxial stress cycling show that all the three

Table 3
Basic mechanical properties of the three rail steels obtained from monotonic tensile tests.

	Elastic modulus, *E* (GPa)	Nominal yield strength, $\sigma_{0.2}$ (MPa)	Ultimate tensile strength, σ_{ult} (MPa)	Elongation at failure (%)	Reduction of area (%)
LAHT	212	1000	1446	11.3	35.87
HE1	203	850	1429	8.5	14.71
HE2	212	905	1384	12	39.5

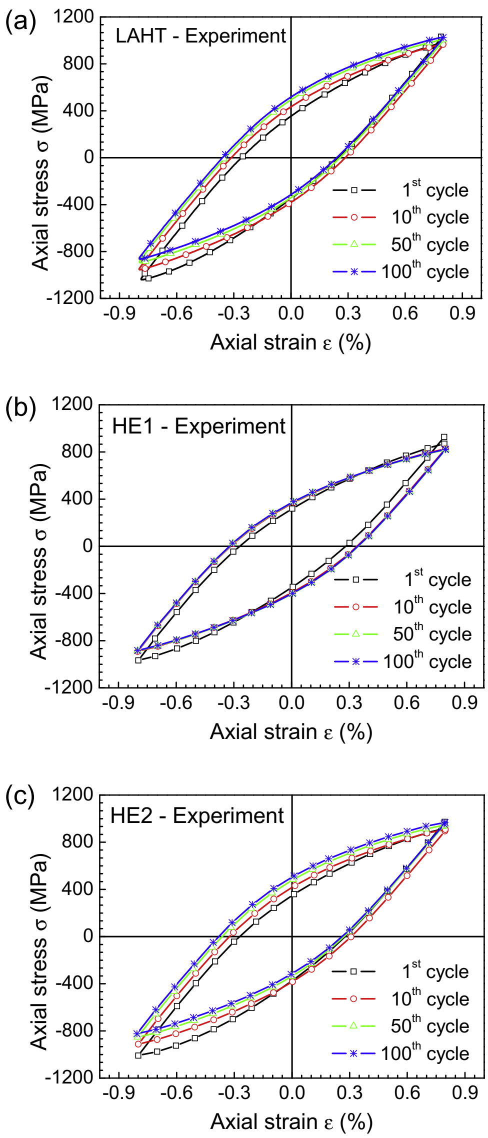

Fig. 5. Cyclic hysteresis stress–strain loops of the (a) LAHT steel; (b) HE1 steel; and (c) HE2 steel under uniaxial symmetrical strain cycling with strain amplitude of 0.8%.

materials behave differently under tension and compression. The accumulated strain under uniaxial cycling loading with tensile mean stress is higher than that with compressive mean stress. This indicates that the materials suffer higher degree of plastic deformation in tensile loading than that in compressive loading. Consequently, the specimen of the LAHT and HE2 steels may suffer higher tensile stress level, which leads to the offset of mean stress

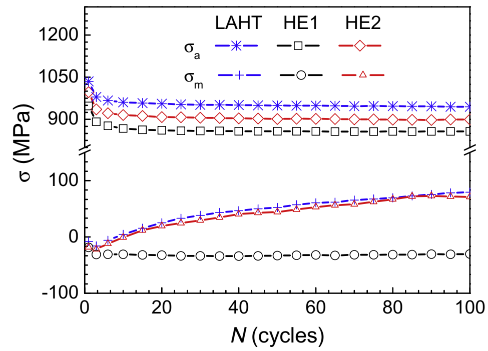

Fig. 6. Diagram of stress amplitude σ_a versus number of loading cycles *N* of all the three rail steels under uniaxial symmetrical strain cycling with strain amplitude of 0.8%.

in the tensile direction, than that of the HE1 materials under the same loading conditions in constant strain range cyclic loading tests.

To clearly identify the cyclic deformation characteristic of the materials under uniaxial strain cycling, the curves of stress amplitude σ_a versus number of loading cycles *N* are shown in Fig. 6. All the three rail steels have a similar response and feature cyclic softening particularly over the first 20 cycles. The stress amplitude decreases almost 8% over the first 10 cycles for the HE1 steel and the HE2 steel and it is of 7.5% over the first 10 cycles for the LAHT steel. The stress amplitude per cycle stabilizes after approximately 20 cycles. The total decrease in stress amplitude over 100 cycles was 10% for all the three rail steels.

Similar tests were carried out by McDowell [34] on ordinary carbon and heat-treated rail steels, both of which had lower nominal strength levels than those used in the current study. Their results show that the stress amplitude of the ordinary carbon rail steel decreases about 6.5% over the first 10 cycles under uniaxial strain cycling at a strain amplitude of 0.9%, and the stress amplitude of the heat-treated rail steel decreases only 3.7% over the first 14 cycles under uniaxial strain cycling at a strain amplitude of 0.6% [34]. A comparison with the current results indicates that the cyclic softening behaviour of the three high strength rail steels used in the current study is greater than that of the ordinary carbon and the heat-treated rail steels examined by McDowell [34]. The tendency for cyclic softening/hardening is also influenced by microstructure, i.e. the density and arrangement of the dislocation structure and substructure of the material [8]. Sunwoo et al. [9] has investigated the cyclic deformation characteristic of pearlitic eutectoid rail steel, and identified an effect of the interlamellar spacing. Their results indicated that a coarser pearlite spacing, i.e. in lower strength grades than being considered here, exhibits cyclic hardening, whereas cyclic softening may occur with a finer pearlite spacing.

2.3.3. Compression–torsion stress cycling

Under the loading paths shown in Figs. 3(a)–(e), the three rail steels were tested under bi-axial compression–torsion stress cycling with different axial stress and equivalent shear stress amplitudes. It is worth noting that the linear and the oblique loading path are the proportional loading paths while the rectangular, the butterfly and the elliptical loading paths are the non-proportional loading paths. Fig. 7 shows the equivalent shear stress $\sqrt{3}\tau$ versus axial strain ε of the three rail steels during the 1st and 100th cycle from the stress cycling with the five studied loading paths at an axial stress amplitude σ_a of −632.5 MPa and equivalent shear stress amplitude $(\sqrt{3}\tau)_a$ of 800 MPa. The results clearly illustrate that the three rail steels feature different ratcheting

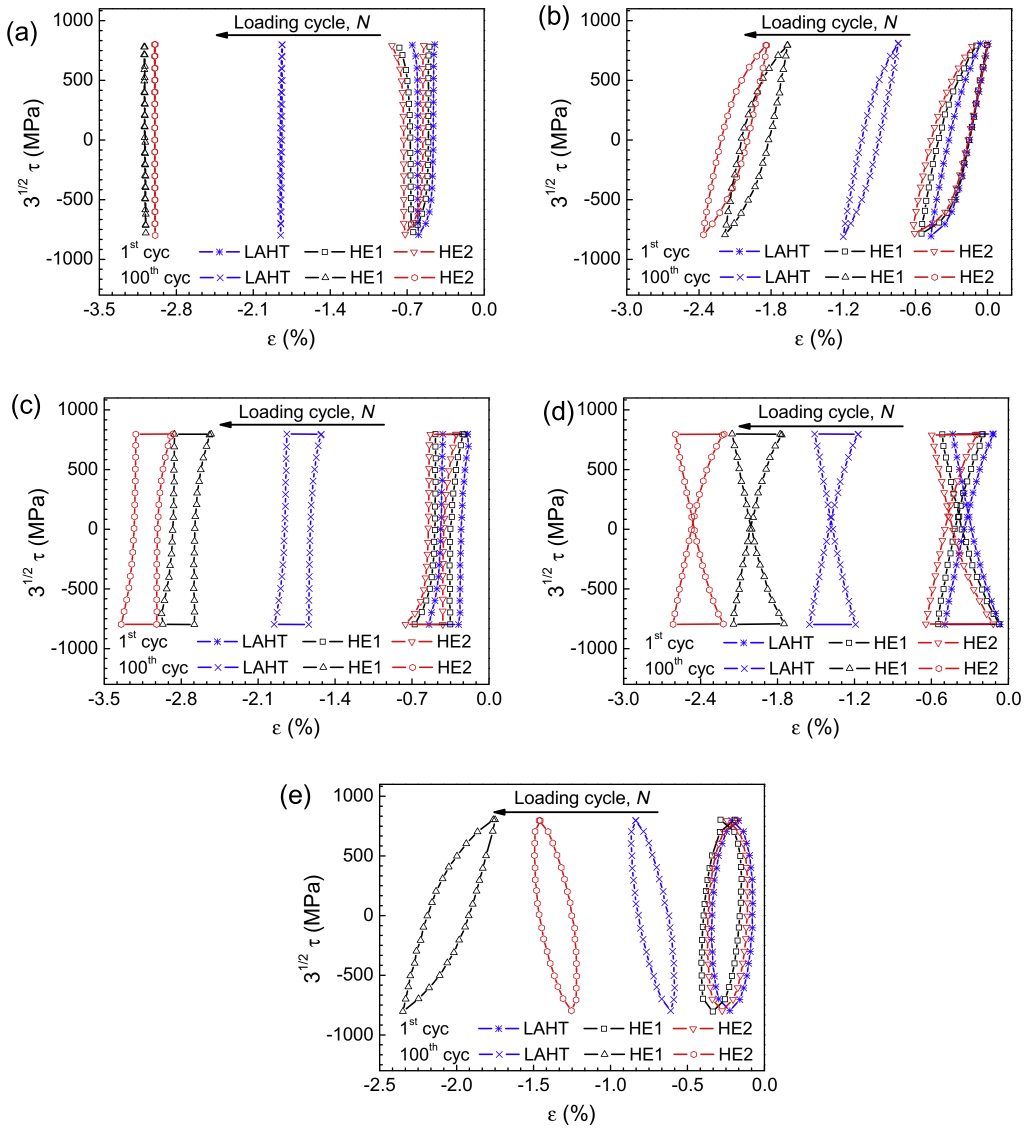

Fig. 7. Experimental results of equivalent shear stress ($\sqrt{3}\tau$) versus axial strain ε of the three studied rail steels during 1st and 100th cycles under (a) linear; (b) oblique; (c) rectangular; (d) butterfly; and (e) elliptical loading paths with the same loading condition of $(\sigma_{eq})_a$ = 1019.8 MPa.

behaviour under the same loading conditions, i.e. the absolute value of ratcheting strain at the 100th cycle for the LAHT steel is the smallest among all the three rail steels for all the cases. Comparison of Fig. 7(a)–(e) also indicates that all the three rail steels exhibit various ratcheting behaviour under different loading paths. It is worth noting that the axial ratcheting is dominant while the torsional ratcheting is relatively small and can be neglected for all the three rail steels under all the five studied loading paths due to the non-zero axial mean stress and the symmetrical torsional stress cycling for all the cases. Fig. 7(a)–(e) shows that the ratcheting of all the three rail steels evolves in the mean stress direction under all the five studied loading paths. Additionally, the hysteresis loop of all the three rail steels changes from an open loop at the 1st cycle to almost a closed loop at the 100th cycle. This implies that all the rail steels stabilize after certain number of loading cycles.

Under the elliptical loading path, the loads are applied 90° out-of-phase. Therefore, the ratio of the torsional stress and the axial stress varies during every single loading cycle. Furthermore, the direction of the maximum shear stress is changing and slip is occurring on different planes at different time during every single loading cycle. This leads to activation of various crystalline slip planes in the materials and results in additional hardening [8]. Consequently, cyclic shift of the hysteresis loops occurred as shown in Fig. 7(e). It was found that the direction of cyclic shift of the hysteresis loop for the HE1 steel is different from that for the LAHT and the HE2 steels. This is possibly due to the difference in the chemical composition, see Table 1, and the microstructure of the materials.

Figs. 8–10 demonstrate the influence of axial stress amplitude σ_a on the ratcheting behaviour of all the three rail steels under the linear loading path while the equivalent shear stress amplitude $(\sqrt{3}\tau)_a$ is kept constant as 1000 MPa. The results show that the same evolution tendency of ratcheting strain and ratcheting strain rate can be found in all the three rail steels. Ratcheting takes place when axial stress amplitude σ_a is high enough. Both axial ratcheting strain ε_r and ratcheting strain rate $d\varepsilon_r/dN$ increase with the axial stress amplitude. Figs. 8 and 9 also demonstrate that the LAHT steel gives the lowest ratcheting strain and the lowest ratcheting strain rate when compared to the other two rail steels under the same loading conditions. In contrast, the HE2 steel has the worst resistance to ratcheting. The ratcheting strain at 100 cycles for

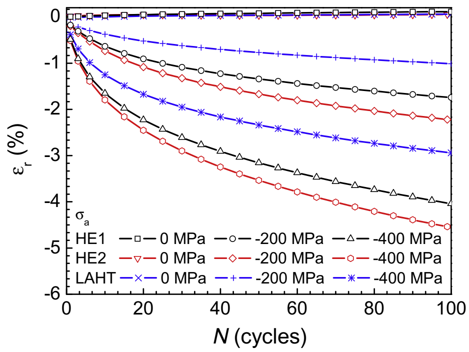

Fig. 8. Axial ratchetting strain ε_r versus number of loading cycles N under linear loading path with different axial stress amplitudes σ_a while the equivalent shear stress amplitude $(\sqrt{3}\tau)_a$ is kept constant.

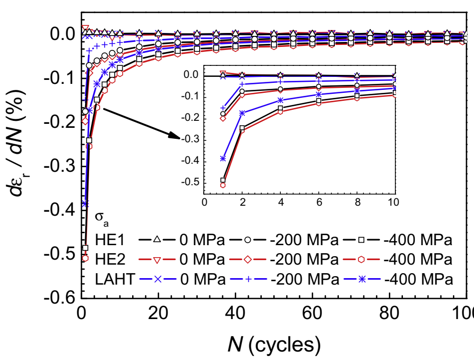

Fig. 9. Axial ratchetting strain rate $d\varepsilon_r/dN$ versus number of loading cycles N under linear loading path with different axial stress amplitudes σ_a while the equivalent shear stress amplitude $(\sqrt{3}\tau)_a$ is kept constant.

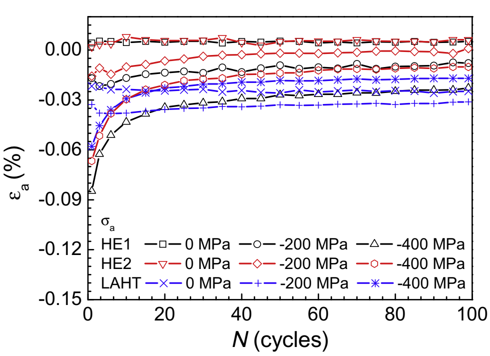

Fig. 10. Axial strain amplitude ε_a versus number of loading cycles N under linear loading path with different axial stress amplitudes σ_a while the equivalent shear stress amplitude $(\sqrt{3}\tau)_a$ is kept constant.

the HE2 steel is up to 55% higher than that found in the LAHT steel under the same loading conditions. Fig. 10 illustrates the axial strain amplitude ε_a of all three rail steels versus number of loading cycles under the linear loading path with different axial stress amplitude. The results show that the strain amplitudes of the two hypereutectoid rail steels, HE1 and HE2 steels, initially decrease followed by maintaining almost constant values. The same evolution tendency of strain amplitude is also found for the LAHT with the axial stress amplitude of −400 MPa, see Fig. 10. For the LAHT steel with the axial stress amplitude of 0 MPa and −200 MPa, the strain amplitude increases in the first few cycles followed by gradually decreases. Additionally, the results show that the strain amplitudes increase with the axial stress amplitude.

The ratcheting behaviour of the materials also depends on the equivalent shear stress amplitude under linear loading path, as shown in Figs. 11–13. For all the cases, the axial stress amplitude σ_a and the mean equivalent shear stress $(\sqrt{3}\tau)_m$ are kept constant as −200 MPa and 0 MPa, respectively. The results indicate that both axial ratcheting strain ε_r and axial ratcheting strain rate $d\varepsilon_r/dN$ increase with the equivalent shear stress amplitude $(\sqrt{3}\tau)_a$, see Figs. 11 and 12. Among all the three rail steels, the LAHT steel has the best resistance to ratcheting as it has the lowest ratcheting strain and ratcheting strain rate. When the equivalent shear stress amplitude equals to 1000 MPa, the HE2 steel gives the highest ratcheting strain which is 55% higher than that for the LAHT steel at 100 cycles. When the equivalent shear stress amplitude is lower than 1000 MPa, the highest ratcheting strain is contributed by the HE1 steel. Fig. 13 shows the axial strain amplitude of all the three rail steels versus number of loading cycles under the linear loading path with different equivalent shear stress amplitudes. The results demonstrate that the strain amplitude increases with the equivalent shear stress amplitude. Furthermore, the strain amplitude decrease followed by gradual increasing with the loading cycle. This indicates that all the three rail steels achieve a stable hysteresis loop after certain number of loading cycles.

The ratcheting behaviour of these three rail steels is significantly influenced not only by the axial stress and equivalent shear stress amplitudes but also by the non-proportional loading path as illustrated in Figs. 14–16. For all the cases, the applied equivalent stress amplitude $(\sigma_{eq})_a$ was kept constant as 1019.8 MPa. The results for all the three rail steels show that the non-proportional loading path influences not only the axial ratcheting strain ε_r but also the axial ratcheting strain rate $d\varepsilon_r/dN$.

Figs. 14(a) and 15(a) show the influence of loading paths on axial ratcheting strain and ratcheting strain rate on the LAHT steel. The results show that the ratcheting strain depends on the loading paths. Among all the five loading paths, the elliptical loading path gives the lowest ratcheting strain and ratcheting strain rate while the linear loading path gives the highest ratcheting strain and rate. Fig. 16(a) demonstrates the influence of different loading path on the strain amplitudes of the LAHT steel. Under the linear and rectangular loading paths, the material exhibit cyclic hardening in the first few cycles and then gradually becomes stable. Under the butterfly loading path, the rail steel exhibits slightly softening followed by hardening and then it gradually becomes stable. Under the oblique and elliptical loading paths, the strain amplitudes remain almost constant, which reveals that the material exhibits cyclic stability.

For the HE1 steel, the highest ratcheting strain and rate are contributed by the linear loading path as shown in Figs. 14(b) and 15(b). The lowest ratcheting strain and rate are relatively difficult to distinguish as the oblique, butterfly and elliptical loading paths give similar ratcheting strain when N is smaller than 60. When N is larger than 60, the lowest ratcheting strain is contributed by the oblique and butterfly loading paths. Fig. 16(b) demonstrates the variation of the strain amplitude of the HE1 steel under different loading path. The results clearly show that the rail steel exhibits slightly hardening in the first few cycles under the linear and the butterfly loading paths while it exhibits slightly softening in the first few cycles under the rectangular and oblique paths. Despite these differences, the material gradually becomes cyclically stable. Under the elliptical path, the material feature cyclic hardening in the first few cycles and gradually becomes stable. However, the material exhibits softening after 40 cycles.

Figs. 14(c) and 15(c) demonstrate the influence of loading path on the ratcheting strain and the ratcheting strain rate of the HE2 steel. In this case, the elliptical loading path gives the lowest ratcheting strain and the lowest ratcheting strain rate. When N is less than 65, the linear loading path gives the highest ratcheting strain.

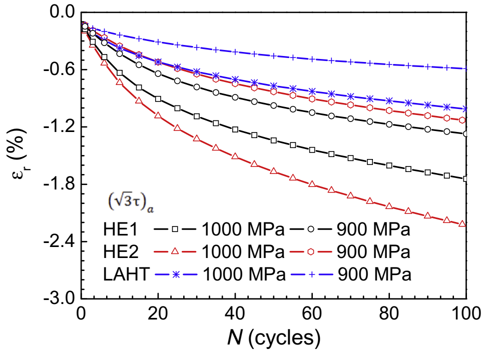

Fig. 11. Axial ratchetting strain ε_r versus number of loading cycles N under linear loading path with different equivalent shear stress amplitudes $(\sqrt{3}\tau)_a$ while the axial stress amplitude is kept constant.

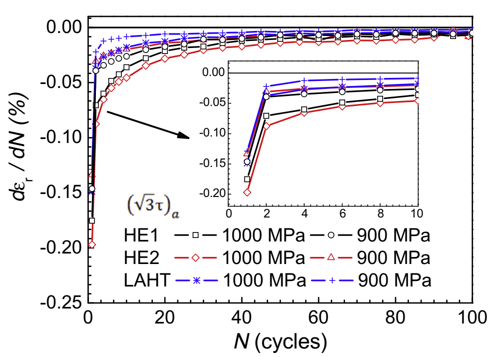

Fig. 12. Axial ratchetting strain rate $d\varepsilon_r/dN$ versus number of loading cycles N under linear loading path with different equivalent shear stress amplitudes $(\sqrt{3}\tau)_a$ while the axial stress amplitude is kept constant.

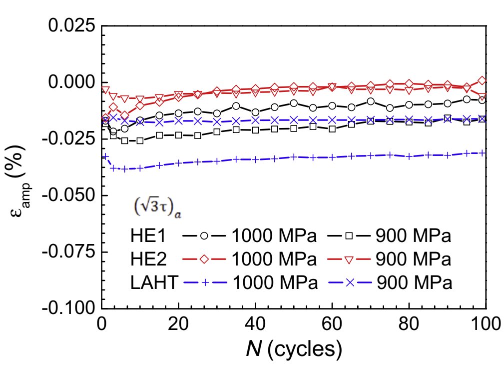

Fig. 13. Axial strain amplitude ε_a versus number of loading cycles N under linear loading path with different equivalent shear stress amplitudes $(\sqrt{3}\tau)_a$ while the axial stress amplitude is kept constant.

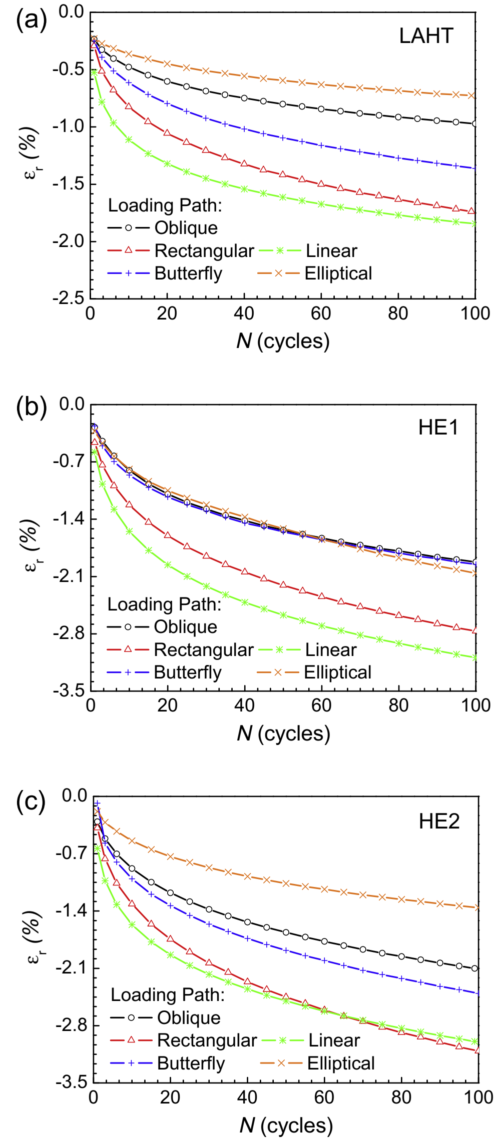

Fig. 14. Axial ratchetting strain ε_r versus number of loading cycles N of the (a) LAHT steel; (b) HE1 steel; and (c) HE2 steel under different non-proportional loading paths while the applied equivalent stress amplitude $(\sigma_{eq})_a$ is kept constant.

When N is larger than 65, the highest ratcheting strain is contributed by the rectangular loading path. Fig. 16(c) illustrates the influence of different loading path on the strain amplitudes of the HE2 steel. The results clearly show that the material exhibits cyclic softening in first few cycles and then becomes almost stable under the butterfly loading path. Under the other four loading paths, the material exhibits cyclic hardening in the first few cycles and then followed by cyclically-stable behaviour.

Figs. 17 and 18 show the comparison of the ratcheting strain and the ratcheting strain rate of these three materials under two non-proportional loading paths, the rectangular and the elliptical loading paths. Among all the three rail steels, the LAHT steel gives the lowest ratcheting strain and the lowest ratcheting strain rate. Under the elliptical loading path, the results clearly show that the highest ratcheting strain is contributed by the HE1 steel while the highest ratcheting strain is contributed by the HE2 steel under the rectangular loading path. The results also indicate that the materials sustain a higher ratcheting strain under the rectangular loading path than that under the elliptical loading path with the same applied equivalent stress amplitude. This is probably due to the hold of a constant axial and torsional stress in the rectangular loading path [16].

Fig. 19 illustrates the variation of strain amplitudes of the three rail steels under the rectangular and the elliptical loading paths. The results clearly show that the LAHT and the HE2 steel behave similarly. Both of them exhibit hardening in the first few cycles and then gradually becomes stable. For the HE1 steel under the rectangular loading path, the strain amplitude initially increases and then decreases with the increase of the cyclic number which reveals that the material exhibits softening initially and then followed by hardening. Under the elliptical loading path, the HE1 steel behaves completely different from the LAHT and the HE2

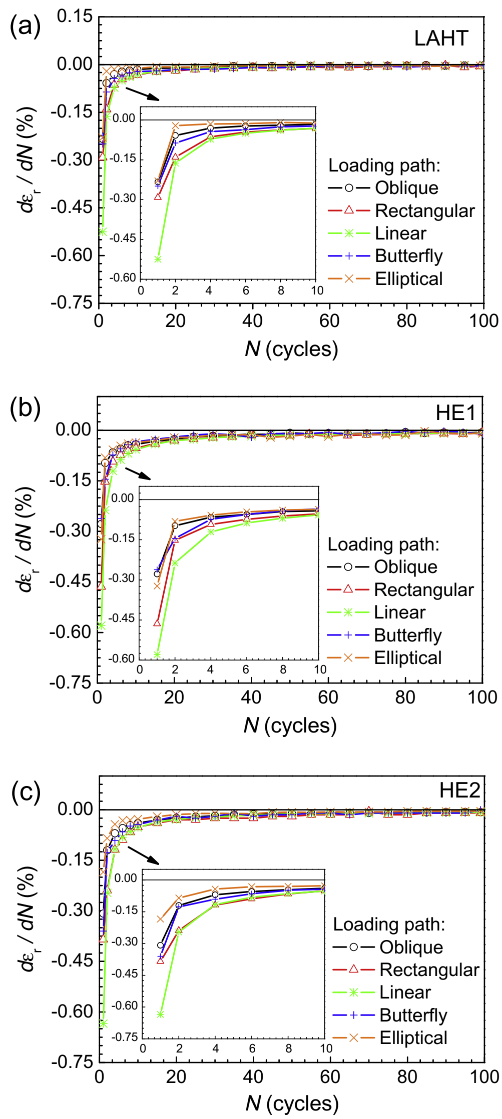

Fig. 15. Axial ratchetting strain rate $d\varepsilon_r/dN$ versus number of loading cycles N of the (a) LAHT steel; (b) HE1 steel; and (c) HE2 steel under different non-proportional loading paths while the applied equivalent stress amplitude $(\sigma_{eq})_a$ is kept constant.

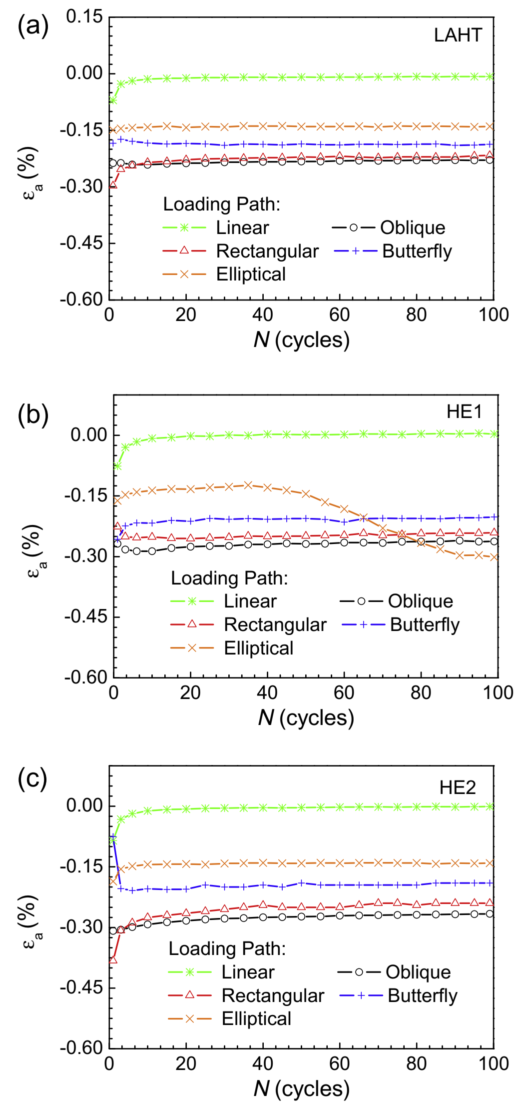

Fig. 16. Axial strain amplitude ε_a versus number of loading cycles N of the (a) LAHT steel; (b) HE1 steel; and (c) HE2 steel under different non-proportional loading paths while the applied equivalent stress amplitude $(\sigma_{eq})_a$ is kept constant.

steel. The HE1 steel exhibits hardening in the first 40 cycles and then softens. This can explain why the shape of the elliptic hysteresis loop of the HE1 steel is different from that of the LAHT and the HE2 steels as shown in Fig. 7(e). Stephens et al. [8] identified that the initially hard or hardened materials tend to soften easier under cyclic loading due to the greater dislocation mobility. Among all the three studied rail steels, the HE1 steel has the highest carbon content of 1% and is the hardest one, and had the highest tendency to exhibit softening under cyclic loading.

The strain amplitudes of the three rail steels at different cyclic number under different loading paths are illustrated in Figs. 16 and 19. It was found that the materials exhibit cyclic softening or cyclic hardening in the first few cycles and then gradually becomes stable in most of the cases. These phenomena may result from the residual work hardening during the manufacturing process of the rail steels. As mentioned above, the accumulated strain varies with the loading paths. When the accumulated strain is small, the residual work hardening cannot be overcome initially and is released by subsequent cycling which leads to cyclic softening. For instance, the HE2 steel subjected to butterfly loading paths gives the lowest ratcheting strain in the first few cycles among all the five studied loading paths, see Fig. 16(c) and it was found that the material exhibits obvious cyclic softening in the first few cycles and then becomes stable quickly. In contrast, the residual work hardening can be overcome when the accumulated strain is high enough and the materials exhibit cyclic hardening. Similar ratcheting behaviour was also investigated for the U71Mn rail steel by Kang et al. [35] under uniaxial strain cycling with different strain amplitudes.

Figs. 8, 9, 11, 12, 14 and 15 demonstrate that the axial ratcheting strain increases but its rate decreases continuously with increasing number of loading cycles. After a certain number of loading cycles, a quasi-steady ratcheting rate is obtained, i.e., the axial ratcheting strain rate becomes very small and remains almost constant in the remaining cycles. It is also found that the increase of axial stress and equivalent shear stress leads to an increase in the required cyclic number to reach quasi-steady ratcheting rate of the material. Besides, the required cyclic number to reach quasi-steady of different material is found to be different, i.e. 20 cycles for the LAHT steel in Fig. 15(a), 45 cycles for the HE1 steel in Fig. 15(b) and 37 cycles for the HE2 steel in Fig. 15(c) under elliptical path. This indicates that the required number of loading cycle for reaching quasi-steady ratcheting rate also depends on the

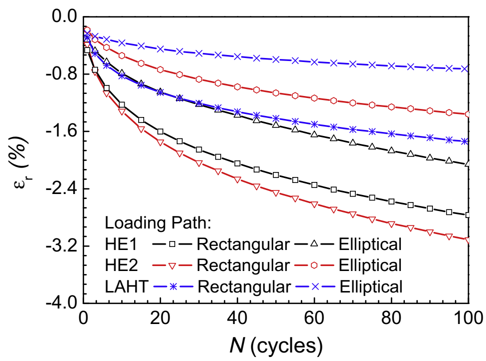

Fig. 17. Comparison of the ratchetting strain ε_r of all the three rail steels under the rectangular path and elliptical path while the applied equivalent stress amplitude $(\sigma_{eq})_a$ is kept constant.

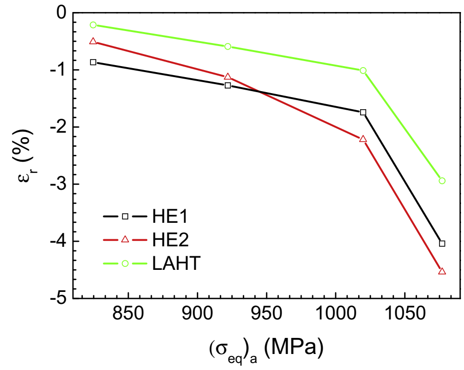

Fig. 20. Comparison of the ratchetting strain ε_r of all the three rail steels under the linear loading path with different equivalent stress amplitude $(\sigma_{eq})_a$.

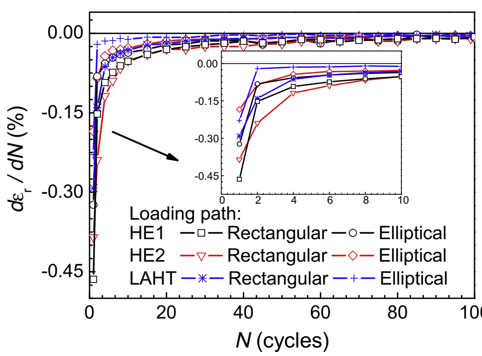

Fig. 18. Comparison of the ratchetting strain rate $d\varepsilon_r/dN$ of all the three rail steels under the rectangular path and elliptical path while the applied equivalent stress amplitude $(\sigma_{eq})_a$ is kept constant.

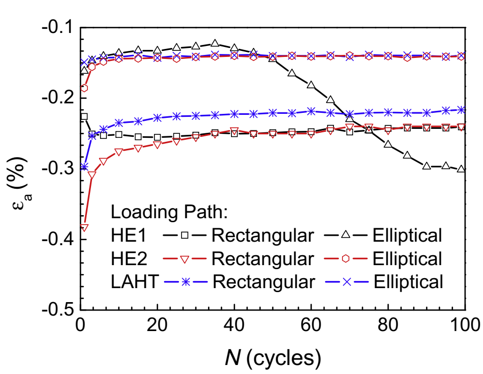

Fig. 19. Comparison of the strain amplitude ε_a of all the three rail steels under the rectangular path and elliptical path while the applied equivalent stress amplitude $(\sigma_{eq})_a$ is kept constant.

material properties. Referring to the experimental results of monotonic tensile tests presented in Section 2.3.1, it is found that the material which gives a higher yield strength requires a larger cyclic number to reach quasi-steady ratcheting rate.

Through the comparison of all the three rail steels under bi-axial compressive–torsion stress cycling with different axial stress and equivalent shear stress amplitudes as well as different multi-axial loading paths, it is found that the LAHT steel always gives the lowest ratcheting strain and the lowest ratcheting strain rate, see Figs. 8, 9, 11, 12, 17, 18, 20 and 21. This indicates that the low alloy heat-treated rail steel grade has a better resistance to ratcheting than that of the hypereutectoid rail steel grades. Figs. 20 and 21 demonstrate the comparison of the ratcheting strain ε_r and the ratcheting strain rate $d\varepsilon_r/dN$ at 100th loading cycle of all the three rail steels under the linear loading path with different applied equivalent stress amplitude $(\sigma_{eq})_a$. Among the two hypereutectoid rail steel grades, the HE1 steel with carbon content of 1% gives a lower ratcheting strain and a lower ratcheting strain rate than the HE2 steel with carbon content of 0.85% if the applied equivalent stress amplitude is high enough, i.e. when the applied equivalent stress amplitude is larger than 930 MPa, and vice versa at a lower equivalent stress amplitude, see Figs. 20 and 21. This comparison indicates that an increase of carbon content in the hypereutectoid rail steel grade can reduce the ratcheting strain development when the rail subjected to severe loading conditions, e.g. in heavy haul operations.

Although biaxial tension–torsion tests were traditionally performed to investigate the ratcheting behaviour of materials, the results in the current study show that material ratcheting also takes place under compression–torsion cyclic loading. The latter loading condition is also closer to that which occurs under normal wheel–rail contact. In the current study, the ratcheting strain rate under multi-axial stress cycling rapidly decreases with an increased number of cycles, which is different from existing cyclic softening materials [16]. The normal and shear stresses responses in numerical simulation of wheel–rail contact patch was found to be elliptical in shape which implies that the relative weak ratcheting behaviour will occur in real wheel/rail rolling contact process. These features and their effect on ratcheting should be taken into account in cyclic constitutive model development in the future.

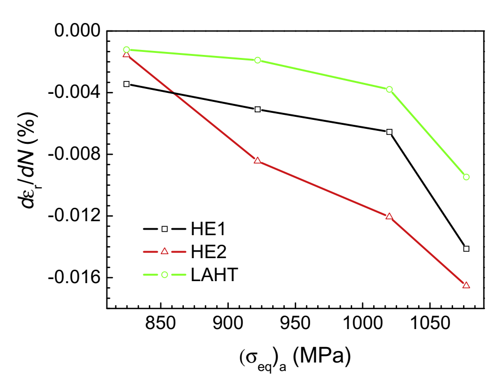

Fig. 21. Comparison of the ratchetting strain rate $d\varepsilon_r/dN$ of all the three rail steels under the linear loading path with different equivalent stress amplitude $(\sigma_{eq})_a$.

Research on ratcheting-fatigue life interaction indicates that the presence of ratcheting not only decreases the fatigue life of materials but also influences the fatigue crack growth due to accumulated plastic strain [16,21,58–61]. The fatigue life of materials strongly depends on the mean stress and the stress amplitude under uniaxial cyclic loading and it depends on the axial stress and the equivalent shear stress amplitudes and the multi-axial loading path under multi-axial cycling loading. Moreover, the interaction behaviour between the ratcheting and the fatigue life of the material was found to be different for different materials. The current study does not investigate the interaction between the ratcheting and the fatigue life of the materials (i.e. the tests were not performed till failure of the materials) as the aim of the study is to investigate and compare the ratcheting behaviour of all the three high strength rail steels under multi-axial cyclic loading. Despite this, it is worth noting that the occurrence of the ratcheting strain does not enhance the fatigue life of the rail steels.

3. Numerical simulation

3.1. A modified cyclic plasticity model for ratcheting

The forementioned experimental results show that there are some similar ratcheting features of the three rail steels under uniaxial strain cycling and biaxial stress cycling. To numerically predict the ratcheting performance of the rail steels in practice, it is essential to apply an appropriate and reliable constitutive model to simulate the cyclic deformation behaviour of the rail steels. Based on the initial isotropic elasticity and associated plastic flow rules at small deformation, the main equations adopted in cyclic plastic constitutive modelling are as follow,

$$\boldsymbol{\varepsilon} = \boldsymbol{\varepsilon}^p + \boldsymbol{\varepsilon}^e \tag{1}$$

$$\boldsymbol{\varepsilon}^e = \mathbf{D}^{-1} : \boldsymbol{\sigma} \tag{2}$$

$$\dot{\boldsymbol{\varepsilon}}^p = \sqrt{\frac{3}{2}}\dot{\lambda}\frac{\mathbf{s} - \boldsymbol{\alpha}}{\|\mathbf{s} - \boldsymbol{\alpha}\|} \tag{3}$$

$$F_y = \sqrt{1.5(\mathbf{s} - \boldsymbol{\alpha}) : (\mathbf{s} - \boldsymbol{\alpha})} - Q \tag{4}$$

where $\boldsymbol{\varepsilon}$, $\boldsymbol{\varepsilon}^e$, $\boldsymbol{\varepsilon}^p$ and $\dot{\boldsymbol{\varepsilon}}^p$ are total strain, elastic strain, plastic strain and plastic strain rate, respectively. $\mathbf{D}$ is the fourth order tensor of elasticity. $\mathbf{s}$ and $\boldsymbol{\alpha}$ are the deviatoric parts of stress and back stress. Q is the isotropic deformation resistance and F_y is the von-Mises yield function. $\dot{\lambda}$ is the rate of plastic multiplier. $\|\ \|$ denotes the norm.

AbdelKarim and Ohno [46] proposed a kinematic hardening rule which combines the Armstrong and Frederick [47] and the Ohno and Wang [40] rules, and was adopted in the current study. The evolution equations of back stress for the kinematic hardening rule is shown as follows,

$$\boldsymbol{\alpha} = \sum_{i=1}^{M}\boldsymbol{\alpha}_i \quad (i = 1, 2, \ldots, M) \tag{5}$$

$$\dot{\boldsymbol{\alpha}}_i = \zeta_i\left[\frac{2}{3}r_i\dot{\boldsymbol{\varepsilon}}^p - \mu_i\boldsymbol{\alpha}_i\dot{p} - H(f_i)\boldsymbol{\alpha}_i\left\langle \dot{\boldsymbol{\varepsilon}}^p : \frac{\boldsymbol{\alpha}_i}{\|\boldsymbol{\alpha}_i\|} - \mu_i\dot{p}\right\rangle\right] \tag{6}$$

where $\boldsymbol{\alpha}_i$ is components of back stress $\boldsymbol{\alpha}$, H is Heaviside function, $\langle\ \rangle$ is Macaulay's bracket and means that: as $x \leqslant 0$, $\langle x\rangle = 0$; as $x > 0$, $\langle x\rangle = x$. $\dot{p}$ is the effective plastic strain rate. The critical state of dynamic recovery is described by the critical surfaces f_i:

$$f_i = \|\boldsymbol{\alpha}_i\|^2 - r_i^2 = 0 \tag{7}$$

The ratcheting parameter μ_i is assumed as a constant for different components of back stress.

$$\mu_i = \mu = \mu_0(1 - a\Phi) \tag{8}$$

where μ_0 is a ratcheting parameter in the uniaxial cases. a is a material parameter reflecting the influence of the non-proportional loading paths on ratcheting behaviour.

As discussed in Section 2, the experimental results have shown that the non-proportionally bi-axial ratcheting behaviour of all the three rail steels strongly depends on the loading paths. Therefore, it is important to consider the non-proportionality of loading path in the cyclic plasticity model. In order to improve the cyclic plasticity model to simulate the non-proportional ratcheting responses, the non-proportional parameter Φ in Eq. (8), initially proposed by Tanaka [62] is implemented into the modified model.

The Tanaka non-proportional parameter has been successfully implemented into some existing constitutive models for the simulation of biaxial cyclic deformation of several materials. Jiang and Kurath [63] modified the Tanaka model [62] to simulate the non-proportional cyclic deformation of the 304 stainless steel and the 1045 steel. Their numerical results showed that the inclusion of the Tanaka non-proportional parameter can significantly improve the accuracy of the simulation of non-proportional cyclic loadings. Similar studies were also carried out by Hassan et al. [64] and Krishna et al. [10] who implemented the Tanaka non-proportional parameter into a modified Chaboche model to improve the biaxial ratcheting simulation. Zhang and Jiang [65] developed a constitutive model by following the Armstrong–Frederick hardening rule with the Tanaka non-proportional parameter. Their results indicated that non-proportional hardening of the pure polycrystalline copper can be captured successfully. Additionally, Krishna et al. [10] investigated that the Tanaka non-proportional parameter is more effective than the Benallal and Marquis [66] parameter in improving the simulation of both ratcheting and evolution tendency of ratcheting.

In current study, the non-proportional parameter Φ is modified in the model through a fourth order tensor $\mathbf{C}$,

$$\dot{\mathbf{C}} = b(\mathbf{n}\otimes\mathbf{n} - \mathbf{C})\dot{p} \tag{9a}$$

$$\Phi = \sqrt{2\left(\frac{tr(\mathbf{C}:\mathbf{C}) - \mathbf{n}:\mathbf{C}:\mathbf{C}:\mathbf{n}}{tr(\mathbf{C}:\mathbf{C})}\right)} \tag{9b}$$

where $\mathbf{n} = \frac{\dot{\boldsymbol{\varepsilon}}^p}{\|\dot{\boldsymbol{\varepsilon}}^p\|}$, b is the rate parameter of the dislocation evolution. $tr(\bullet)$ is the trace of a tensor. The tensor $\mathbf{C}$ describes the slow growth of the internal dislocation structure induced by the plastic deformation process, its components equal to zero for an initially isotropic material and reach the target value $\mathbf{n}\otimes\mathbf{n}$ that depends on the plastic strain direction of the loading. Therefore, the non-proportional factor Φ is associated with the non-proportional loading path and history. For proportional uniaxial loadings, $\Phi = 0$; for a non-proportional circular path, $\Phi \approx 1$; for the other non-proportional multi-axial loading paths, their non-proportional factor satisfies $0 < \Phi < 1$. It is worth noting that the original non-proportional parameter Φ proposed by Tanaka [62] approaches $1/\sqrt{2}$ for a non-proportional circular path.

Basically, the cyclic softening rule adopted in the cyclic plasticity model is used with the combined hardening model which considers both isotropic and kinematic hardening rules to capture the cyclic softening feature and the ratcheting behaviour. In order to consider the effects of loading history and non-proportional loading path, the following evolution equations for the isotropic deformation resistance Q are adopted in the constitutive model,

$$\dot{Q} = \gamma(Q_{sa} - Q)\dot{p} \tag{10a}$$

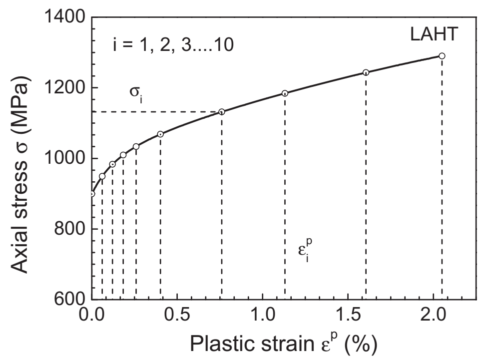

Fig. 22. Uniaxial stress σ versus plastic strain ε^p from the monotonic loading test of the LAHT rail steel for calibrating the back stress of the cyclic plasticity model.

Table 4
Calibrated material parameters used in the modified plasticity model for the three rail steels.

	HE1	HE2	LAHT
$\zeta_1, \zeta_2, \zeta_3, \zeta_4$	1820, 926, 498, 331	900, 389, 174, 90	1470, 3110, 1350, 556
$\zeta_5, \zeta_6, \zeta_7, \zeta_8$	188, 110, 77.5, 30.6	55.2, 41.3, 34.1, 24.4	286, 112, 80, 35.6
r_1, r_2, r_3, r_4 (MPa)	24.1, 83.6, 68.9, 62	109, 102, 62.4, 55.1	177, 23.1, 44.9, 53.3
r_5, r_6, r_7, r_8 (MPa)	66.9, 59.1, 31.2, 440	56.5, 69.1, 44.8, 194	56.2, 47.4, 35.3, 344
E (GPa), υ, μ_0	203, 0.33, 0.05	212, 0.33, 0.01	212, 0.33, 0.045
Q_0, Q_{sa0}, Q_{sa1} (MPa)	650, 400, 440	680, 550, 660	630, 460, 600
a, c, γ	0.7, 50, 2.0	0.7, 50, 1.0	0.7, 50, 2.0

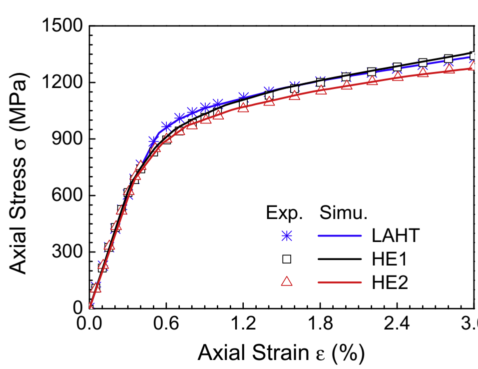

Fig. 23. Comparison between the experimental and simulated results of the stress–strain response under monotonic tensile test for the three rail steels.

$$Q_{sa}(\Phi) = \Phi[Q_{sa1} - Q_{sa0}] + Q_{sa0} \tag{10b}$$

where $Q_{sa}(\Phi)$ is saturated isotropic deformation resistance relating to non-proportional factor Φ, and γ is a material parameter to control the evolution rate of Q_{sa}. Q_{sa0} and Q_{sa1} are the saturated isotropic deformation resistance under the cyclic loading paths for $\Phi = 0$ and $\Phi \approx 1$, respectively. The initial value of Q is denoted as Q_0.

3.2. Calibration of material parameters

In current study, the simulated results of uniaxial and multi-axial ratcheting of one of the studied rail steels, the LAHT rail steel, are compared with the corresponding experimental results to

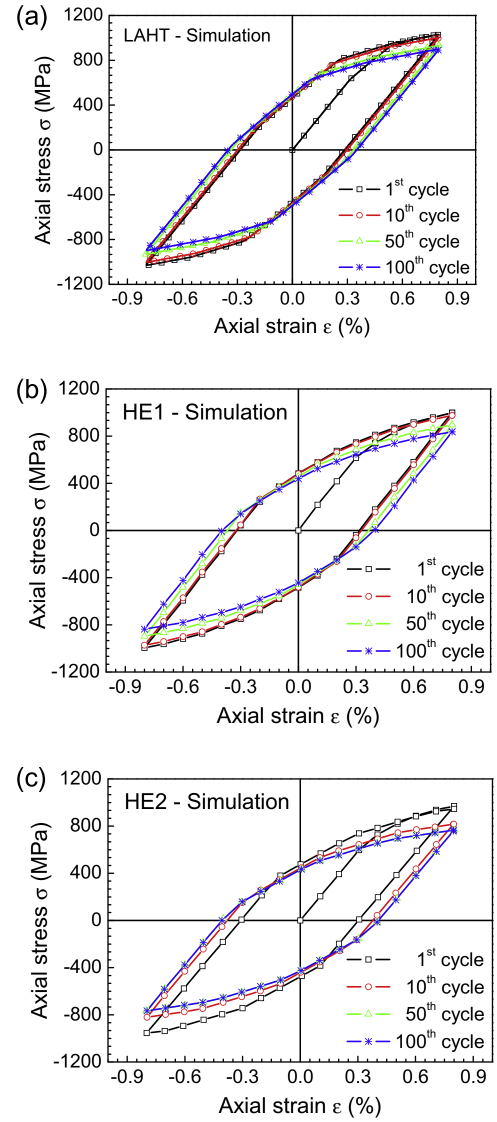

Fig. 24. Simulated cyclic stress–strain hysteresis loops of the (a) LAHT steel; (b) HE1 steel; and (c) HE2 steel under uniaxial symmetrical strain cycling with strain amplitude of 0.8%.

examine the capability of the cyclic plasticity model described in Section 3.1. Parameter calibration for applying the cyclic plasticity model was performed by non-linearly fitting the experimental results of uniaxial strain cycling and monotonic tensile test. The method to calibrate the material parameters is presented below.The material constants ζ_i and r_i used to describe the evolution of the back stress in Eq. (6) of the cyclic plasticity model can be determined by,

$$\begin{cases} \zeta_i = \frac{1}{\varepsilon_i^p} \\ r_i = \left(\frac{\sigma_i - \sigma_{i-1}}{\varepsilon_i^p - \varepsilon_{i-1}^p} - \frac{\sigma_{i+1} - \sigma_i}{\varepsilon_{i+1}^p - \varepsilon_i^p}\right)\varepsilon_i^p \end{cases} \tag{11}$$

where σ_i and ε_i^p are the yield stress and the corresponding plastic strain obtained from a stress–plastic strain curve of a monotonic tensile test after the isotropic softening was removed, as did in [67]. As an example, Fig. 22 shows how a set of 10 data pair (σ_i, ε_i^p) are extracted from the stress–plastic strain curve of the LAHT rail steel for using Eq. (11) to calibrate 8 pairs of (ζ_i, r_i).

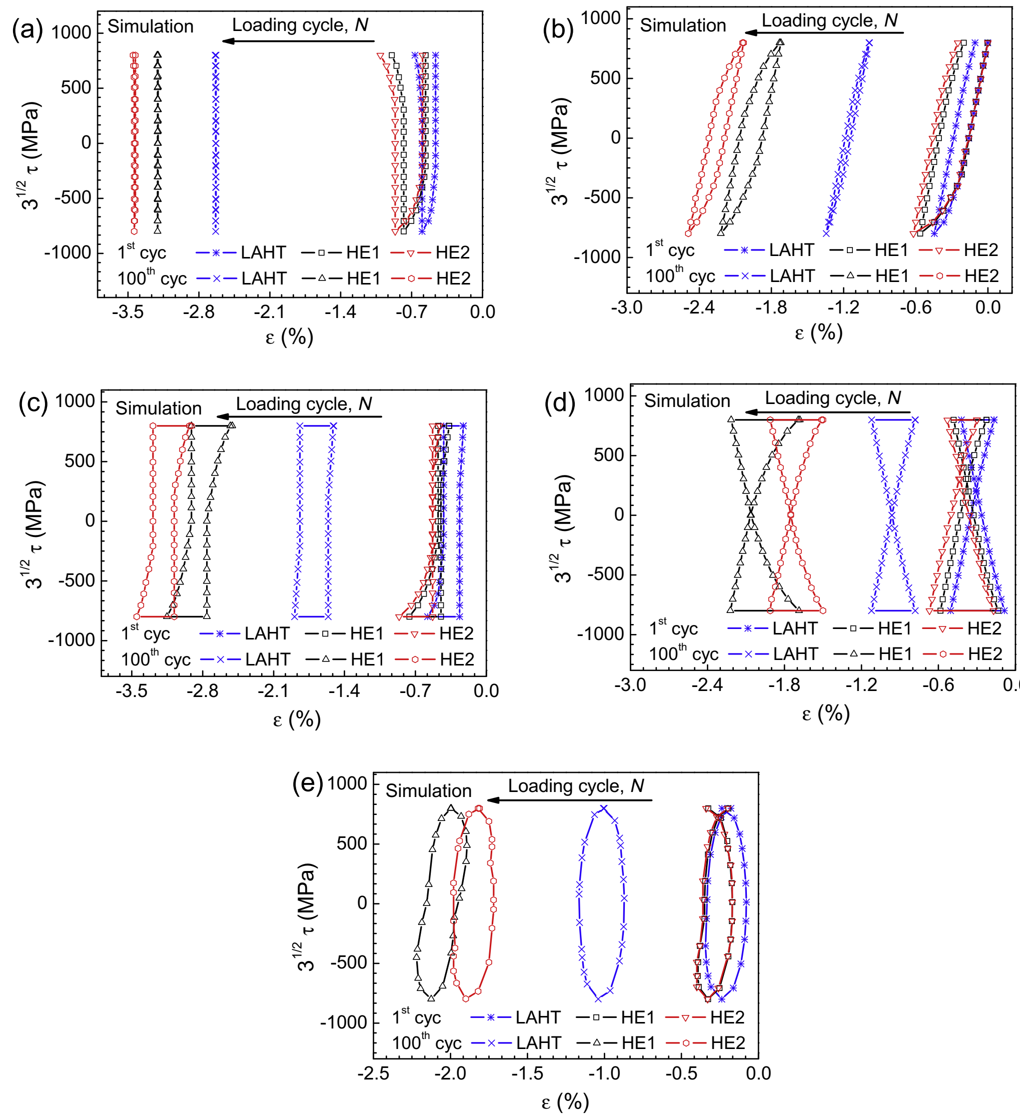

Fig. 25. Simulated results of equivalent shear stress $\sqrt{3}\tau$ versus axial strain ε of the three rail steels under (a) linear path; (b) oblique path; (c) rectangular path; (d) butterfly path; and (e) elliptical path.

The control parameter γ is assumed to be a constant for uniaxial and bi-axial loadings and can be obtained by fitting the curve of the equivalent stress amplitude σ_a^{eq} versus the number of cycles N by the following equation:

$$\sigma_a^{eq} = A_1 + A_2[1 - \exp(-\gamma N)] \quad (12)$$

where A_1, A_2 are fitting parameters. When the material reaches cyclic saturation at a certain accumulated plastic strain, the saturated isotropic deformation resistances of Q_{sa0} can be calculated by

$$Q_{sa0} = Q_0 - (\sigma_a^{eq}|_{N=1} - A_1 - A_2) \quad (13)$$

where $\sigma_a^{eq}|_{N=1}$ is the equivalent stress amplitude at first cycle. Q_{sa1} can be obtained by trial–error method from the bi-axial stress cycling due to lack of the experimental data of the bi-axial symmetrical strain cycling. The ratcheting parameters, μ_0 reflecting the kinematic hardening in the uniaxial case, can be determined by an optimizing process, i.e.:

$$\delta(\mu_0) = \sum_{k=1}^{n} \left| \frac{\varepsilon_r^{\exp} - \varepsilon_r^{simu}}{\varepsilon_r^{\exp}} \right|_k \quad (14)$$

where $\varepsilon_r^{\exp}$ and ε_r^{simu} are experimental and simulated ratcheting strains at a certain cycle (i.e., 100th cycle in the present study), respectively. k is the number of uniaxial loading cases. The parameter μ_0 can be obtained from the minimum value of $\delta(\mu_0)$. The parameter a, which reflects the influence of non-proportional loading path on the parameter μ shown in Eq. (8), is assumed as a constant for all non-proportional loading paths and can be obtained from fitting an arbitrary non-proportional path. The parameter b represents the rate of dislocation evolution, which affects the first few cycles and reaches rapidly a stable value at a certain non-proportional loading path. Therefore, it is assumed as a constant and can be optimized from different non-proportional loading paths, similar to Eq. (14) for calibrating μ_0. It is noted that the parameter μ_0 has almost no influence on uniaxial tensile and strain cycling results and should be determined first. Finally, the material parameters obtained for all the three rail steels are summarized in Table 4.

3.3. Simulations of uniaxial strain cyclic loading

With the material parameters listed in Table 4, the applicability of the cyclic plasticity model as described in Section 3.1 was first verified by simulating the monotonic tensile tests. The simulated stress–strain responses of all the three rail steels are shown in Fig. 23, which agree well with the corresponding experimental results. After that, the uniaxial strain cycling of the three rail steels was simulated numerically. Figs. 5 and 24 show the experimental and simulated stress–strain curves of the three rail steels under uniaxial strain cycling, respectively. The results show that the simulated results agree with the experimental results fairly well for the values of the stress in valleys although there are some differences in the shapes of hysteresis loops. Furthermore, the stress amplitudes obtained from the simulated results are in reasonable agreement with the experiments. It is worth noting that the cyclic softening behaviours of the materials, i.e. stress amplitude σ_a decreases with the increase of loading cycles, has been successfully captured by the simulations.

3.4. Simulations of bi-axial stress cyclic loading

The modified cyclic plasticity model with the calibrated material data was applied to simulate the bi-axial stress cycling with different non-proportional loading paths. The simulated axial strain-torsional stress curves under the five studied loading paths of all the three rail steels are shown in Fig. 25 and compared with the corresponding experimental results shown in Fig. 7. The results show that the simulated hysteresis loops are similar to the experimental ones. Additionally, the predicted axial ratcheting strain ε_r at different number of loading cycles from all different loading paths is presented in Fig. 26 and compared with corresponding experimental results.

Fig. 26(a) shows the comparison for the LAHT steel and it indicates that the ratcheting strain is slightly over predicted in the case of the oblique loading path. Despite this, the overall simulated results are in a reasonable agreement with the experiment and the shapes of the hysteresis loops are similar. For the butterfly loading path, the evolution tendency of ratcheting can be captured by the modified cyclic plasticity model fairly well although the axial ratcheting strain is underpredicted slightly. For the other three loading paths, the comparison shows that the simulations agree well with the corresponding experimental results.

Comparisons between the numerical results and the experimental results for the HE1 steel are shown in Fig. 26(b). The numerical results demonstrate that the evolution tendency of the ratcheting strain is not simulated well in the case of the rectangular loading path. Despite this, the ratcheting strain value at 100th cycle is similar to the experimental results. For the linear loading path, the overall simulated results give a reasonable agreement with the experimental results although slight overprediction of the ratcheting strain is found. The results also illustrate that the model can give a reasonable prediction of ratcheting strain value in the case of the butterfly path though slight underprediction is found at the start of the simulation. For the oblique and the elliptical paths, the comparison shows that the simulations agree well with the corresponding experimental results.

Fig. 26(c) illustrates the comparisons for the HE2 steel. The results show that the ratcheting behaviour of this rail steel under butterfly path cannot be simulated as well as the other two rail steels. The value of the ratcheting strain is underpredicted about 30%. Despite this, the overall simulated results of the HE2 steel under other four loading paths give a reasonable agreement with the experimental results. The ratcheting strain is slightly overpredicted for the linear loading path while the ratcheting strain is slightly underpredicted for the elliptical loading path. For the oblique and the rectangular loading paths, the comparison shows that the simulations agree well with the corresponding experimental results for the values of the axial ratcheting strain.

The predicted axial strain amplitude ε_a at different number of loading cycles from all the different loading paths are presented in Fig. 27 and compared with corresponding experimental results. Fig. 27(a) illustrates the comparisons for the LAHT steel. The comparison clearly demonstrates that the simulated evolution tendency and strain amplitude values for the linear loading path agree well with the experimental results. For the oblique and the rectangular loading paths, the strain amplitude is overestimated. The simulated results for the butterfly and the elliptical paths give a reasonable agreement with the experimental results although slight differences are found in the first few cycles. Fig. 27(b) demonstrates the comparisons of the axial strain amplitude between the numerical results and the experimental results. The results show that the simulation for the linear loading agrees well with the experimental results. The evolution tendency and the values of axial strain amplitude for the other cannot be simulated well, especially for the elliptical path. The decrease of strain amplitude after 40th cycle cannot be captured in the simulation. Despite this, the ratio of overprediction or underprediction of strain amplitudes for the other three loading paths is small and acceptable. Fig. 27(c) shows the comparison for the HE2 steel. The comparison show that the simulation for the linear loading path agrees well with the corresponding experimental results for the values of axial strain amplitude although slight overprediction is found in the first few

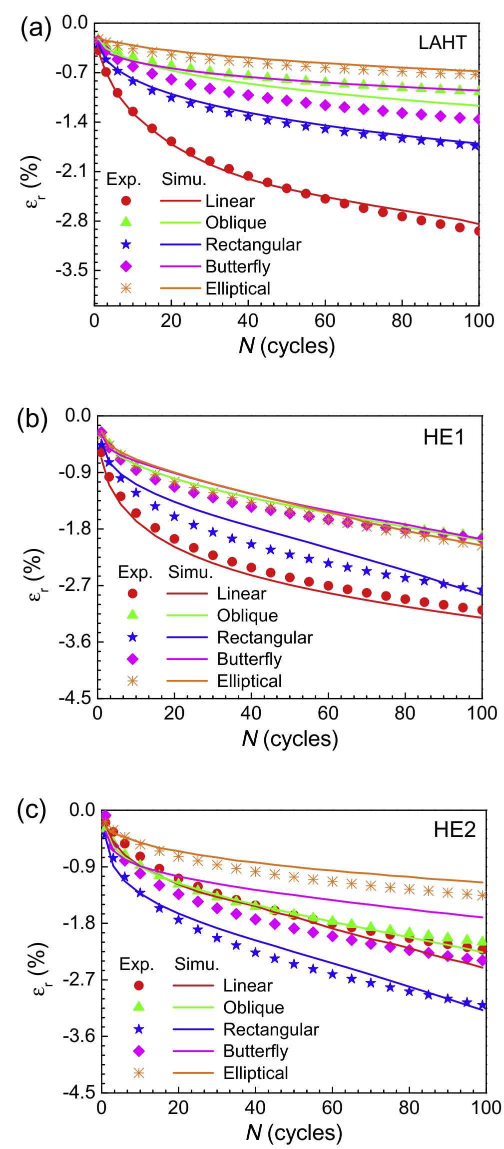

Fig. 26. Experimental and simulated ratchetting strain by the proposed model under biaxial cyclic loadings for the (a) LAHT steel; (b) HE1 steel; and (c) HE2 steel.

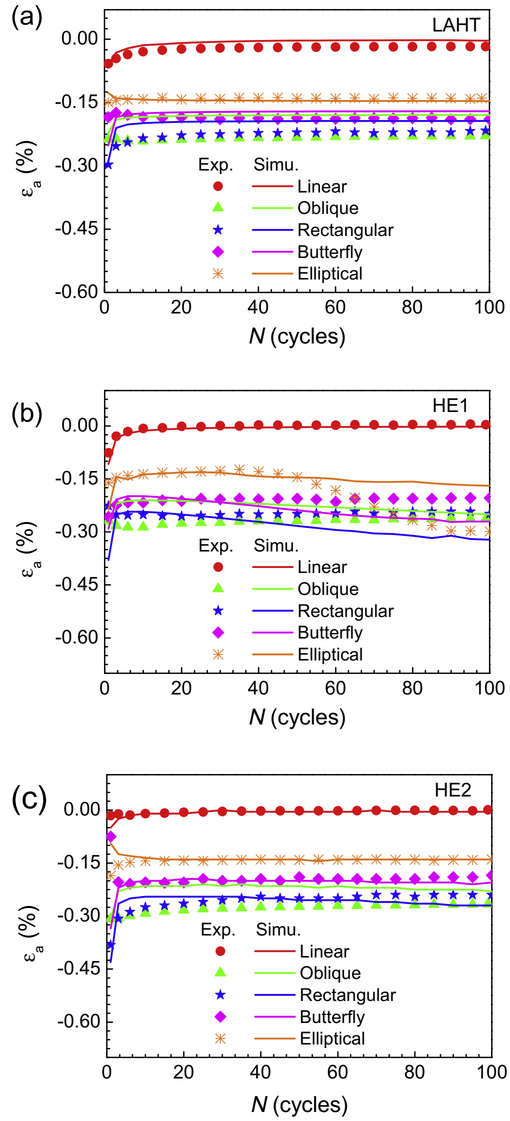

Fig. 27. Experimental and simulated strain amplitude by the proposed model under biaxial cyclic loadings for the (a) LAHT steel; (b) HE1 steel; and (c) HE2 steel.

cycles. For the oblique loading path, the evolution tendency agrees well with the experimental results but the values of strain amplitude are slightly underpredicted. For the rectangular loading path, the simulated results agree fairly well with the experimental results. For the butterfly and the elliptical loading paths, differences are found in the first few cycles. Despite this, the overall simulated results give a reasonable agreement with the experimental results.

Although discrepancies can be found in the prediction of the axial ratcheting strain and axial strain amplitudes, especially for the HE1 steel, as shown in Figs. 26 and 27, the overall simulated results of the ratcheting strain values for all three rail steels are in a reasonable agreement with the experiment as the ratio of overprediction or underprediction is small for most cases, i.e. less than 10%. This is due to the introduction of the non-proportionally multi-axial parameter Φ into the isotropic and kinematic hardening rules. Additionally, the evolution tendency of ratcheting can be captured by the modified cyclic plasticity model fairly well and the shapes of the hysteresis loops are similar to the experimental results, see Figs. 25 and 26. This indicates that the modified cyclic plasticity model can be applied to quantify ratcheting strain of these hypereutectoid rail steels under bi-axial cyclic loadings with acceptable accuracy. The suggested method of calibrating the material parameters from the experimental study can also be applied to calibrate the material parameters of other rail steels. Furthermore, this cyclic plasticity model with the calibrated material data from the experimental study can be applied to simulate actual wheel–rail rolling contact to investigate ratcheting performance of different rail steel in practice in our future work.

4. Conclusions

Three high strength, heat treated rail steels, a low alloy heat-treated (LAHT) rail steel grade and two hypereutectoid rail steel grades with different carbon contents (HE1 steel for the higher carbon content rail steel and HE2 steel for the lower carbon content rail steel), which are currently used in heavy haul operations in Australia, have been tested under uniaxial strain cycling and bi-axial compression–torsion cyclic loading conditions. Under uniaxial symmetrical strain cycling, all the three materials exhibit cyclic softening at the start and then stabilize quickly as the stress amplitude of all three materials decreases almost 8% over the first 10 cycles for the HE1 steel and the HE2 steel and it is of 7.5% over the first 10 cycles for the LAHT steel before reaching a stable value.

Under multi-axial stress cycling, the ratcheting behaviour of these materials is significantly influenced by the axial stress and the equivalent shear stress amplitudes and the non-proportional loading path. Both ratcheting strain and ratcheting strain rate increase with axial stress and equivalent shear stress amplitudes. A quasi-steady ratcheting rate reaches after a certain number of loading cycles. This quasi-steady number of loading cycles is influenced by axial stress and equivalent shear stress amplitudes as well as material's yield strength. Among all the five studied loading paths, the elliptical loading path, which is more relevant to wheel/rail contact situations, gives the lowest ratcheting strain and the lowest ratcheting strain rate. Comparing all the three rail steels, it has been found that the low alloy heat-treated rail steel grade has the best resistance to ratcheting. Among the two hypereutectoid rail steel grades, the one with a higher percentage of carbon content gives a lower ratcheting strain and ratcheting strain rate if the rail is subjected to a higher equivalent stress amplitude, e.g. in heavy haul operations. Besides, the ratcheting strain rate under multi-axial stress cycling rapidly decreases with an increased number of cycles, which is different from existing cyclic softening materials.

A modified cyclic plasticity model was applied to simulate the ratcheting behaviour of the rail steels under experimental loading conditions. The method for calibrating the material parameters required by the modified model is presented and the material parameters for all the three studied rail steels were determined from the experimental data. The comparison between the simulated results and the experimental data show that the modified cyclic plasticity model has the capacity to simulate both uniaxial and biaxial ratcheting behaviour of the studied rail steels with an acceptable accuracy. It provides the confidence for the future work to apply this constitutive model to study the actual wheel/rail rolling contact in practice.

Acknowledgement

The present work has been partly funded by an Australian Research Council Linkage Project (LP110100655) with support from Rio Tinto Iron Ore.

References

[1] Cannon DF, Edel D-O, Grassie SL, Sawley K. Rail defects: an overview. Fatigue Fract Eng Mater Struct 2003;26:865–87.

[2] Wen Z, Wu L, Li W, Jin X, Zhu M. Three-dimensional elastic–plastic stress analysis of wheel–rail rolling contact. Wear 2011;271:426–36.
[3] Olver AV. The mechanism of rolling contact fatigue: an update. Proc IMechE Part J: J Eng Tribol 2005;219:313–30.
[4] Kapoor A. Wear by plastic ratchetting. Wear 1997;212:119–30.
[5] Kapoor A. A re-evaluation of the life to rupture of ductile metals by cyclic plastic strain. Fatigue Fract Eng Mater Struct 1994;17:201–19.
[6] Tyfour WR, Beynon JH, Kapoor A. Deterioration of rolling contact fatigue life of pearlitic rail due to dry-wet rolling–sliding line contact. Wear 1996;197:255–65.
[7] Su X, Clayton P. Ratchetting strain experiments with a pearlitic steel under rolling/sliding contact. Wear 1997;205:137–43.
[8] Stephens RI, Fatemi A, Stephens RR, Fuchs HO. Metal fatigue in engineering. 2nd ed. New York: John Wiley and Sons; 2001.
[9] Sunwoo H, Fine ME, Meshii M, Stone DH. Cyclic deformation of pearlitic eutectoid rail steel. Metall Trans A 1982;13A:2035–47.
[10] Krishna S, Hassan T, Naceur IB, Saï K, Cailletaud G. Macro versus micro-scale constitutive models in simulating proportional and non-proportional cyclic and ratcheting responses of stainless steel 304. Int J Plast 2009;25:1910–49.
[11] Hassan T, Kyriakides S. Ratcheting of cyclically hardening and softening materials: I. Uniaxial behavior. Int J Plast 1994;10(2):149–84.
[12] Hassan T, Kyriakides S. Ratcheting of cyclically hardening and softening materials: II. Multiaxial behavior. Int J Plast 1994;10(2):185–212.
[13] Jiang Y, Zhang J. Benchmark experiments and characteristic cyclic plasticity deformation. Int J Plast 2008;24:1481–515.
[14] Taleb L. About the cyclic accumulation of the inelastic strain observed in metals subjected to cyclic stress control. Int J Plast 2013;43:1–19.
[15] Xiong Y, Yu Q, Jiang Y. An experimental study of cyclic plastic deformation of extruded ZK60 magnesium alloy under uniaxial loading at room temperature. Int J Plast 2013;53:107–24.
[16] Kang G, Liu Y, Ding J. Multiaxial ratchetting–fatigue interactions of annealed and tempered 42CrMo steels: experimental observations. Int J Fatigue 2008;30:2104–18.
[17] Kang G, Liu Y, Ding J, Gao Q. Uniaxial ratcheting and fatigue failure of tempered 42CrMo steel: damage evolution and damage-coupled visco-plastic constitutive model. Int J Plast 2009;25:838–60.
[18] Kang G, Gao Q, Cai L, Sun Y. Experimental study on uniaxial and nonproportionally multiaxial ratcheting of SS304 stainless steel at room and high temperatures. Nucl Eng Des 2002;216:13–26.
[19] Kang G, Gao Q, Yang X. Uniaxial and non-proportionally multiaxial ratcheting of SS304 stainless steel at room temperature: experiments and simulations. Int J Non-linear Mech 2004;39:843–57.
[20] Kang G, Kan Q, Zhang J, Sun Y. Time-dependent ratchetting experiments of SS304 stainless steel. Int J Plast 2006;22:858–94.
[21] Kang G, Liu Y, Li Z. Experimental study on ratchetting–fatigue interaction of SS304 stainless steel in uniaxial cyclic stressing. Mater Sci Eng A 2006;435–436:396–404.
[22] Hassan T, Kyriakides S. Ratcheting of cyclic plasticity, part I. Uniaxial behavior. Int J Plast 1992;8:91–116.
[23] Hassan T, Kyriakides S. Ratcheting of cyclic plasticity, part II. Multiaxial behavior. Int J Plast 1992;8:117–46.
[24] Jiang Y. An experimental study of inhomogeneous cyclic plastic deformation. J Eng Mater Technol 2001;123:274–80.
[25] Zhang J, Jiang Y. An experimental study of inhomogeneous cyclic plastic deformation of 1045 steel under multiaxial cyclic loading. In J Plast 2005;21:2174–90.
[26] Jiang Y, Huseyin S. Cyclic ratcheting of 1070 steel under multiaxial stress states. Int J Plast 1994;10:608–79.
[27] Jiang Y, Huseyin S. Multiaxial cyclic ratcheting under multiple step loading. Int J Plast 1994;10:849–70.
[28] Portier L, Calloch S, Marquis D, Geyer P. Ratcheting under tension–torsion loadings: experiments and modelling. Int J Plast 2000;16:303–35.
[29] Kang GZ, Gao Q, Cai LX, Yang XJ, Sun Y. Experimental study on uniaxial and multiaxial strain cyclic characteristics and ratcheting of 316L stainless steel. J Mater Sci Technol 2001;17(2):219–23.
[30] Date S, Ishikawa H, Otani T, Takahashi Y. Effect of ratcheting deformation on fatigue and creep-fatigue life of 316FR stainless steel. Nucl Eng Des 2008;238:336–46.
[31] Bower AF. Cyclic hardening properties of hard-drawn copper and rail steel. J Mech Phys Solids 1989;37(4):455–70.
[32] Lim CB, Kim KS, Seong JB. Ratcheting and fatigue behaviour of a copper alloy under uniaxial cyclic loading with mean stress. Int J Fatigue 2009;31:501–7.
[33] Kim CY, Song JH, Hwangbo Y, Shim HS. Plastic deformation behavior of Cu thin films during fatigue testing. Procedia Eng 2010;2:1421–30.
[34] McDowell DL. Stress state dependence of cyclic ratcheting behaviour of two rail steels. Int J Plast 1995;11(4):397–421.
[35] Kang GZ, Gao Q, Yang XJ. Experimental study on the cyclic deformation and plastic flow of U71Mn rail steel. Int J Mech Sci 2002;44:1647–63.
[36] Kang GZ, Gao Q. Uniaxial and non-proportionally multiaxial ratcheting of U71Mn rail steel: experiments and simulations. Mech Mater 2002;34:809–20.
[37] Chaboche JL. Time-independent constitutive theories for cyclic plasticity. Int J Plast 1986;2:149–88.
[38] Chaboche JL. On some modifications of kinematic hardening to improve the description of ratcheting effects. Int J Plast 1991;7:661–78.
[39] Chaboche JL. Modeling of ratchetting: evaluation of various approaches. Eur J Mech A/Solids 1994;13:501–18.
[40] Ohno N, Wang J-D. Kinematic hardening rules with critical state of dynamic recovery, part I: formulations and basic features for ratcheting behaviour. Int J Plast 1993;9:375–90.
[41] Ohno N. Recent progress in constitutive modelling for ratchetting. Mater Sci Res Int 1997;3(1):1–9.
[42] Bari S, Hassan T. Anatomy of coupled constitutive models for ratcheting simulation. Int J Plast 2000;16:381–409.
[43] Bari S, Hassan T. An advancement in cyclic plasticity modelling for multiaxial ratcheting simulation. Int J Plast 2002;18:873–94.
[44] Jiang Y, Sehitoglu H. Modeling of cyclic ratchetting plasticity, Part I: development of constitutive relations. ASME J Appl Mech 1996;63:720–5.
[45] Voyiadjis GZ, Basuroychowdhury IN. A plasticity model for multiaxial cyclic loading and ratchetting. Acta Mech 1998;126:19–35.
[46] AbdelKarim M, Ohno N. Kinematic hardening model suitable for ratcheting with steady-state. Int J Plast 2000;16:225–40.
[47] Armstrong PJ, Frederick CO. A mathematical representation of the multiaxial Bauschinger effect. CEGB report RD/B/N731, Berkely Nuclear Laboratories, Berkely, UK; 1966.
[48] Burlet H, Cailletaud G. Numerical techniques for cyclic plasticity at variable temperature. Eng Comput 1986;3:143–53.
[49] Döring R, Hoffmeyer J, Seeger T, Vormwald M. A plasticity model for calculating stress–strain sequences under multiaxial nonproportional cyclic loading. Comput Mater Sci 2003;28:587–96.
[50] Chen X, Jiao R, Kim KS. On the Ohno–Wang kinematic hardening rules for multiaxial ratcheting modelling of medium carbon steel. Int J Plast 2005;21:161–84.
[51] Kang GZ, Ohno N, Nebu A. Constitutive modelling of strain-range-dependent cyclic hardening. Int J Plast 2003;19:1801–19.
[52] Kang GZ, Li YG, Gao Q. Non-proportionally multiaxial ratcheting of cyclic hardening materials at elevated temperatures: experiments and simulations. Mech Mater 2005;37:1101–18.
[53] Yaguchi M, Takahashi Y. Ratcheting of viscoplastic material with cyclic softening, part 2: application of constitutive models. Int J Plast 2005;21:835–60.
[54] Kan QH, Kang GZ, Zhang J. A unified visco-plastic constitutive model for uniaxial time-dependent ratchetting and its finite element implementation. Theor Appl Fract Mech 2007;47:133–44.
[55] Szablewski D, Kalay S, LoPresti J. Development and evaluation of high performance rail steels for heavy haul operations. In: Proceedings of the 2011 international heavy haul association conference, Calgary, Canada, 19–22 June; 2011.
[56] Szablewski D, Gutscher D, LoPresti J, Kalay S. Effect of heavy axle loads on super premium rail steels and rail joining methods. In: Proceedings of the 10th international heavy haul association conference, New Delhi, India, 4–6 February; 2013. p. 43–50.
[57] The American Railway Engineering and Maintenance-of-Way Association (AREMA). Manual for railway engineering, vol. 1. AREMA; 2012 [chapter 4].
[58] Rider RJ, Harvey SJ, Chandler HD. Fatigue and ratcheting interactions. Int J Fatigue 1995;17(7):507–11.
[59] Xia Z, Kujawski D, Ellyin F. Effect of mean stress and ratcheting strain on fatigue life of steel. Int J Fatigue 1996;18(5):335–41.
[60] Yang X. Low cycle fatigue and cyclic stress ratcheting failure behaviour of carbon steel 45 under uniaxial cyclic loading. Int J Fatigue 2005;27:1124–32.
[61] Tong J, Zhao LG, Lin B. Ratcheting strain as a driving force for fatigue crack growth. Int J Fatigue 2013;46:49–57.
[62] Tanaka E. A nonproportionality parameter and a cyclic viscoplasitc constitutive model taking into account amplitude dependences and memory effects of isotropic hardening. Eur J Mech A/Solids 1994;13:155–73.
[63] Jiang Y, Kurath P. Nonoproportional cyclic deformation: critical experiments and analytical modelling. Int J Plast 1997;13(8–9):743–63.
[64] Hassan T, Taleb L, Krishna S. Influence of non-proportional loading on ratcheting responses and simulations by two recent cyclic plasticity models. Int J Plast 2008;24:1863–89.
[65] Zang J, Jiang Y. Constitutive modelling of cyclic plasticity deformation of a pure polycrystalline copper. Int J Plast 2008;24:1890–915.
[66] Benallal A, Marquis D. Constitutive equations for nonproportional cyclic elasto-viscoplasticity. ASME J Eng Mater Technol 1987;109:326–36.
[67] Kang GZ, Gao Q, Yang XJ. A viscoplastic constitutive model incorporated with cyclic hardening for uniaxial/multiaxial ratcheting of SS304 stainless steel at room temperature. Mech Mater 2002;34:521–31.